S.-T. Yau High School Science Award

Research Report

Physics

The Team

Name of team member: Ziyi Cui

School: University of Toronto Schools

City, State/Province, Country: Toronto, Ontario, Canada

Instructor

Prof. Richard M. Lueptow

Job Title: Professor

Institution: Northwestern University

City, Country: Evanston, Illinois, USA

Title of Research Report

Collision Geometry and Energy-Controlled Fracture in a Three-Sphere Ball-Milling Model

Date

September 14, 2026

Collision Geometry and Energy-Controlled Fracture in a Three-Sphere Ball-Milling Model

Ziyi Cui

Abstract

We numerically investigate the collision and fracture processes of ball milling in a three-sphere geometry using discrete element method (DEM) simulations combined with Christensen-type and Weibull-type normalized fracture criteria. The outcome of the brittle ore particle (ejected versus trapped, fractured versus intact) depends on the impact geometry and velocity. We develop a reduced three-sphere collision model in which trapping is governed by impact geometry and friction, while fracture inside the trapped regime is governed by an effective impact velocity. The proposed geometry-dependent effective velocity collapses the simulated fracture response across impact angle, obliquity angle, velocity, and particle size ratio: across $300{,}000$ randomized collisions, including $293{,}700$ trapped cases, the reduced-order fracture condition classifies the DEM-derived outcomes within the trapped domain with 99.43% accuracy for the Christensen criterion and 99.29% for the Weibull criterion, with the main discrepancies within a few percent of the fracture threshold and at the fringe of the trapping window.

Keywords: ball milling ; discrete element method ; fracture ; trapping condition ; Weibull theory ; Christensen criterion

Acknowledgement

Ziyi Cui carried out the research presented in this report under academic guidance. His work included developing and implementing the discrete element method simulations, performing the analytical derivations, conducting the numerical analysis and validation, preparing the figures, and drafting the research report.

The project was conducted under the faculty guidance of Prof. Paul B. Umbanhowar and Prof. Richard M. Lueptow at Northwestern University, with research mentoring from Dr. Qiong Zhang and Dr. Suwei Liu. The advisors and mentors provided guidance on the research direction and methodology, discussed the analysis and interpretation of the results, and reviewed the manuscript. Ziyi Cui thanks all four for their guidance and feedback throughout the project.

Commitments on Academic Honesty and Integrity

We hereby declare that we

1. are fully committed to the principle of honesty, integrity and fair play throughout the competition.
2. actually perform the research work ourselves and thus truly understand the content of the work.
3. observe the common standard of academic integrity adopted by most journals and degree theses.
4. have declared all the assistance and contribution we have received from any personnel, agency, institution, etc. for the research work.
5. undertake to avoid getting in touch with assessment panel members in a way that may lead to direct or indirect conflict of interest.
6. undertake to avoid any interaction with assessment panel members that would undermine the neutrality of the panel member and fairness of the assessment process.
7. observe the safety regulations of the laboratory(ies) where we conduct the experiment(s), if applicable.
8. observe all rules and regulations of the competition.
9. agree that the decision of YHSA is final in all matters related to the competition.

We understand and agree that failure to honour the above commitments may lead to disqualification from the competition and/or removal of reward, if applicable; that any unethical deeds, if found, will be disclosed to the school principal of team member(s) and relevant parties if deemed necessary; and that the decision of YHSA is final and no appeal will be accepted.

(Signatures of full team below)

Ziyi Cui

Name of team member: Ziyi Cui

Date: September 14, 2026

Name of supervising teacher:
Prof. Richard M. Lueptow

Date: September 14, 2026 .

Table of Contents

Acknowledgement ii

Commitments on Academic Honesty and Integrity iii

1 Introduction 1

2 Methods 2

2.1 Notation Conventions . . . 2

2.2 Three-Sphere Collision Geometry . . . 2

2.3 DEM Implementation . . . 3

2.4 Fracture Criteria . . . 5

3 Model 8

3.1 Impact Condition . . . 8

3.2 Trapping Condition . . . 9

3.3 Stress State of a Trapped Particle and Critical Contact Forces . . . 10

3.4 Energy-Based Critical Velocity . . . 11

3.5 Model Summary . . . 15

4 Results and Discussion 15

4.1 Effect of Collision Geometry on Fracture . . . 15

4.2 Effect of Friction . . . 17

4.3 Effect of Size Ratio . . . 18

4.4 Comparison of Christensen and Weibull Predictions . . . 18

4.5 Further Validation of the Analytical Model . . . 20

5 Conclusions 22

References 23

Supplementary Information 27

S1 Nomenclature 27

S2 Derivation of the energy–geometry factor 28

S2.1 Contact kinematics . . . 28

S2.2 Quasi-static equilibrium . . . 29

S2.3 Reduction to a single oscillator . . . 31

S2.4 Energy partition . . . 35

S3 Derivation of the damping factor Ψ_{trap} **36**

S3.1 Setup and inputs 36

S3.2 The damped contact law 37

S3.3 A damped linear oscillator 38

S3.4 Exact map: damped Hertz to the linear oscillator 40

S3.5 Peak total force of a binary damped contact: $\Psi_{\text{bin}}(e)$ 41

S3.6 The trapped three-body configuration: $\Psi_{\text{trap}}(e, R)$ 44

S4 Numerical convergence of the recording interval **47**

1 Introduction

Grinding is a critical process applied in a wide range of industries, including mineral processing [1], cement [2], ceramics [3], food [4], pharmaceuticals [5], and the beneficiation of rare-earth metals [6]. Despite its broad application, ball milling is among the least efficient industrial operations [7]. Comminution alone consumes up to 4% of global industrial electricity [8] and approximately 36% of a mine's total power usage [9], yet less than 1% of the input energy actually produces new surface area, with the remainder dissipated as heat, noise, and vibration [10–12]. This inefficiency raises operating costs and magnifies environmental impacts, including increased carbon emissions [13–15]. Because grinding is so widely adopted, even modest efficiency improvements would translate into substantial energy and cost savings while reducing greenhouse gas emissions.

To connect the physics of individual collisions with large-scale milling, previous studies have used experiments to measure breakage. Single-particle impact tests [16], drop-weight experiments [17], and pilot-scale mill trials [18] measure the strength and probability of breakage under controlled loading. These studies reveal real material behavior but cannot practically span the wide range of impact geometries, size ratios, and frictional conditions seen in industrial mills, and scaled-up experiments are costly, time-intensive, and often difficult to reproduce. Theoretical approaches such as population balance models describe particle size distributions across milling time and are computationally efficient [12], but they rely heavily on empirical fitting and do not resolve the mechanics of individual collisions, which are the actual triggers of fracture [19]. In short, experiments provide realism but narrow scope, population balance models provide generality but limited physical detail.

Numerical simulation offers a way to overcome some of these limitations. The discrete element method (DEM) has become one of the most versatile tools for studying granular materials [20–24] because it explicitly resolves particle trajectories, contact forces, and energy dissipation [25, 26] by treating each particle as a discrete entity and integrating its motion under Newton's laws. Unlike population balance models, DEM does not require empirical fitting to capture local collision mechanics; unlike experiments, DEM can systematically sweep impact velocity, angle, size ratio, and friction over a range of values that is difficult to achieve in the laboratory. At the same time, simulation outcomes are most powerful when interpreted together with theoretical models that encode the governing physics, so that DEM and theory together provide both predictive capability and particle-level insight.

This study develops a simulation-theory framework in which the collision outcome is separated into two stages that can be analyzed independently. The first stage is geometric and frictional: whether the target particle is trapped between a pair of grinding balls or is ejected before it can be loaded. The second stage is energetic: whether a trapped particle experiences sufficient compressive loading to fracture. A three-sphere collision system is used to represent the local environment of a ball mill while allowing precise control of impact velocity v, impact angle α, obliquity angle γ, size ratio R, and friction coefficient μ. Trapping is governed by a closed-form geometric condition that generalizes the classical angle-of-nip criterion of roll-crusher and high-pressure grinding-roll theory to a three-sphere geometry [27–30], while fracture within the trapped regime is evaluated with two normalized failure criteria applied to the DEM output, one a global stress-based limit state and one a local, flaw-controlled tensile criterion: a Christensen failure function built from the virial stress tensor and a Weibull failure function built from the contact forces. By combining DEM with analytic models, this study provides both detailed numerical

results and a compact mechanistic picture that sheds light on improving grinding efficiency in mineral processing, rare-earth extraction, and pharmaceutical manufacturing.

2 Methods

2.1 Notation Conventions

A complete symbol list is given in Supplementary Section S1. Scalars are set in italic (v, F, θ), vectors in upright bold ($\mathbf{v}$, $\mathbf{F}_i$), unit vectors carry a hat ($\hat{\mathbf{n}}_1$, $\hat{\mathbf{n}}_a$), and second-order tensors in bold italic ($\bar{\boldsymbol{\sigma}}$). Indexed components follow the summation convention (σ_{kk}, $s_{ij}s_{ij}$).

Contact quantities carry n or t for the normal and tangential directions: F_i^n and F_i^t are the normal and tangential force at contact i, δ and δ_t the corresponding relative displacements, and k_n and k_t the spring stiffnesses. The branch vector $\boldsymbol{\ell}_i$ runs from the target particle center to contact i, and $\mathbf{T}_i$ is the torque it exerts.

Subscripts t and g denote the target particle and the grinding balls (m_t, ρ_g, ψ_t, ψ_g); the contact subscript t for "tangential" appears only on contact quantities, where no body label is possible. Superscripts C and W denote quantities belonging to the Christensen and Weibull criteria respectively, and a star denotes an effective or reduced quantity in the Hertzian contact model (R^*, E^*, m^*). E^* is the effective Young's modulus, whereas energies are written E with a descriptive subscript (E_{kin}, E_{el}, E_{mode}). V denotes volume only and $\mathbf{U}$ displacement only.

2.2 Three-Sphere Collision Geometry

Fig. 1 shows the three-sphere collision in this study. Two identical grinding balls have radius $r_g = 25$ mm, and the smaller target particle, used as a representative material to be broken up, has radius r_t. One grinding ball is fixed and centered at $\mathbf{C}_f$, initially tangent to the target particle at $\mathbf{C}_t$; *fixed* here means that this ball can neither translate nor rotate, as distinct from a stationary ball, whose velocity is zero but which is free to move. The other grinding ball, centered at $\mathbf{C}_i$, travels with initial velocity $\mathbf{v}$ until it contacts the target particle. It begins a short distance away and travels at constant velocity, so that the collision starts at the instant of first contact.

Two contacts, $\mathbf{C}_f - \mathbf{C}_t$ and $\mathbf{C}_i - \mathbf{C}_t$ happen at the same time with the contact forces $\mathbf{F}_1$ and $\mathbf{F}_2$, located at the branch vectors $\boldsymbol{\ell}_1 = -r_t\hat{\mathbf{n}}_1$ and $\boldsymbol{\ell}_2 = -r_t\hat{\mathbf{n}}_2$, each of length r_t, drawn from the center of the target particle to its two contact points. Unit vector $\hat{\mathbf{n}}_1$ points from $\mathbf{C}_f$ to $\mathbf{C}_t$ and $\hat{\mathbf{n}}_2$ from $\mathbf{C}_i$ to $\mathbf{C}_t$; these are the directions of the normal forces exerted on the target particle. The corresponding axes are the lines that carry these unit vectors: the n_1 axis passes through $\mathbf{C}_f$ and $\mathbf{C}_t$, and the n_2 axis through $\mathbf{C}_i$ and $\mathbf{C}_t$. The impact angle α is measured between $\mathbf{v}$ and the n_1 axis, and the obliquity angle γ between $\mathbf{v}$ and $\hat{\mathbf{n}}_2$. Positive angles are counterclockwise about the out-of-plane unit normal $\hat{\mathbf{z}}$.

The parameter ranges are $v \in [0.5, 5]$ m/s, $\alpha \in [-90°, 90°]$, $\gamma \in [0°, 90°)$, $R = r_g/r_t \in [2, 20]$, and $\mu \in [0, 1]$. The size ratio R is varied by changing r_t while holding r_g fixed. The velocity range spans the shell speeds of real ball mills, which set the scale of the grinding-media velocities: the 25.4 cm laboratory batch mill of Datta and Rajamani [31] turns at 55 rpm, a shell speed of 0.73 m/s, while the 5 m industrial mill of Cleary [32], 4.8 m inside the liners, has a critical speed of 19.5 rpm, giving a shell speed of 4.9 m/s

at the critical speed and 3.7 m/s at the 75% of critical typical of operation. The grinding ball and target particle sizes are drawn from the same setting: the charge of that mill consists of 50–100 mm steel balls and 5–50 mm rock, against 50 mm balls and 2.5–25 mm target particles here.

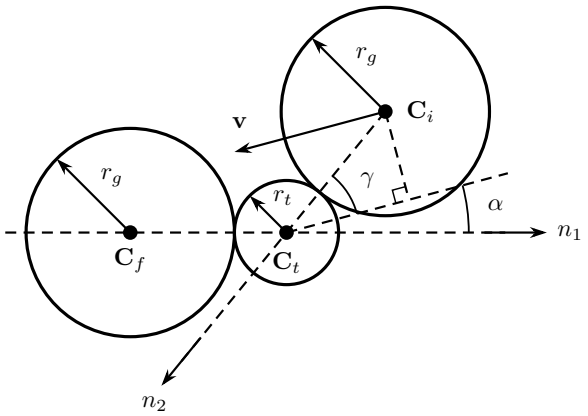


Figure 1: Schematic of the three-sphere collision. A fixed grinding ball (center $\mathbf{C}_f$, radius r_g) is tangent to a smaller brittle target particle (center $\mathbf{C}_t$, radius r_t), while a second grinding ball (center $\mathbf{C}_i$, radius r_g) approaches with velocity $\mathbf{v}$. The dashed horizontal line through $\mathbf{C}_f$ and $\mathbf{C}_t$ defines the n_1 axis, and the dashed ray through $\mathbf{C}_t$ drawn parallel to $\mathbf{v}$ makes the impact angle α with n_1. The line of centers $\mathbf{C}_t\mathbf{C}_i$ defines the n_2 axis and forms the obliquity angle γ with the dashed ray parallel to $\mathbf{v}$. A dashed perpendicular from $\mathbf{C}_i$ to this ray is shown with a right-angle marker, indicating the offset $(r_g + r_t)\sin\gamma$.

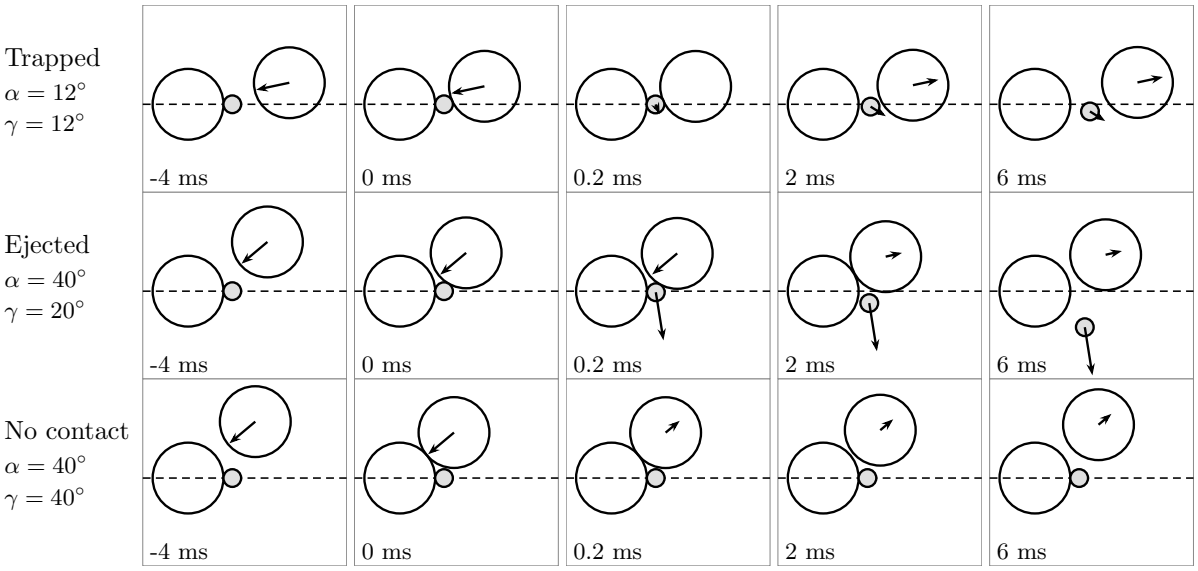
The DEM simulations show that, depending on the impact geometry, the target particle is either not contacted at all, ejected from between the two grinding balls, or trapped between them (Fig. 2(a)). Only the trapped particle is substantially loaded, as shown by the compressive stress in the target particle versus time in Fig. 2(b). The conditions under which each outcome occurs are derived in Section 3.

2.3 DEM Implementation

The three-sphere dynamics are simulated with the open-source LAMMPS package [33]. Contacts are modeled using Hertz's model with a contact restitution coefficient [34] in the normal direction and the history-dependent Mindlin model [26] limited by Coulomb sliding friction in the tangential direction. The tangential dashpot is disabled ($\eta_t = 0$), so tangential dissipation occurs through Coulomb sliding alone; the tangential stiffness is derived from E and ν rather than prescribed independently, so the properties of Table 1 fix the contact model completely. Corresponding to a common ball milling setup, we use limestone for the target particle material and steel for the grinding balls. Although the analysis here is for steel grinding balls and a limestone target particle, the approach applies to any target particle material or grinding ball material. Table 1 lists the material and contact properties [35–37], with subscripts t and g denoting the target particle and grinding balls, respectively. Based on the same-material sliding friction coefficients in Table 1, LAMMPS assigns the geometric average $\mu = 0.47$ to the limestone–steel contact.

No measured value of the limestone–steel restitution coefficient could be located in the literature, so $e = 0.50$ is adopted as a plausible value for both contact pairs. Section 3.4 and Supplementary Section S3 quantify the sensitivity of the fracture threshold to this choice. The equations of motion are integrated with the synchronized velocity-Verlet scheme [38] with a timestep of $\Delta t = 1.0 \times 10^{-7}$ s, resolving each binary contact with hundreds of timesteps over the investigated material and size ranges. Output is

(a)



(b)

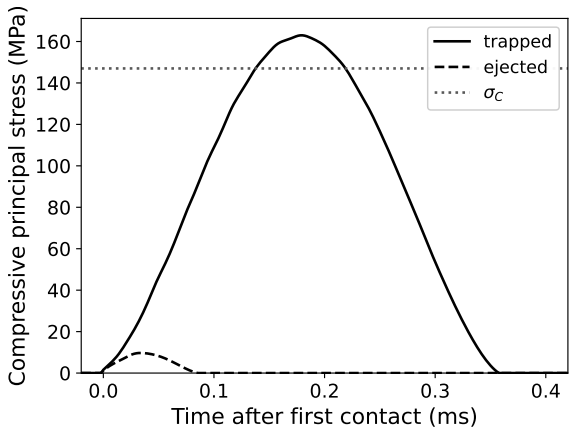


Figure 2: (a) DEM snapshots for $v = 3$ m/s, $R = 4$ ($r_g = 25$ mm, $r_t = 6.25$ mm), and $\mu = 0.47$. Three rows are shown, labeled at left with the outcome and (α, γ): trapped ($\alpha = 12°$, $\gamma = 12°$), ejected ($\alpha = 40°$, $\gamma = 20°$), and no contact ($\alpha = 40°$, $\gamma = 40°$). Time is measured from the first contact of the incoming grinding ball. Five snapshots are shown in each row at -4, 0, 0.2, 2, and 6 ms, with the time printed in each frame. The fixed grinding ball (left) and incoming grinding ball are drawn as open circles, the target particle is the small shaded circle, and the dashed horizontal line is the n_1 axis. The arrows are the velocity vectors of the incoming grinding ball and the target particle, with length proportional to speed. (b) Most compressive principal stress of the target particle, computed from its volume-averaged stress tensor, versus time after first contact for the trapped case (solid) and the ejected case (dashed). The dotted horizontal line is the uniaxial compressive strength of limestone, $\sigma_C = 147$ MPa.

recorded every 100 timesteps; at this interval, the recovered force and stress peaks are converged to within 0.1% (Supplementary Section S4). Each run is integrated from launch through first contact and for an additional 5000 timesteps (0.5 ms), which exceeds the contact duration everywhere in the parameter range. Configurations in which the incoming grinding ball never reaches the target particle are recorded as non-contact events.

Table 1: Material and contact properties used in the LAMMPS simulations.

Property	Symbol	Target particle (limestone)	Grinding ball (steel)
Density (kg m^{-3})	ρ	2700 [35]	7800 [36]
Young's modulus (GPa)	E	77.82 [35]	208 [36]
Poisson's ratio	ν	0.28 [35]	0.27 [37]
Coefficient of restitution	e	0.50	0.50
Sliding friction coefficient	μ_s	0.75 [37]	0.30 [37]
Tangential damping ratio	η_t	0	0

2.4 Fracture Criteria

Fracture can occur only when the target particle is trapped and compressed, as indicated by the compressive stress in the target versus time in Fig. 2(b). The particle fracture in this study is the fragmentation process in which cracks form, propagate across the particle, and split the whole target particle into a few smaller pieces, rather than chipping near the contact points [39]. Although the DEM simulations do not tell us about fracture directly, based on the resolved forces, we detect fracture using two different fracture criteria at different scales and compare the results. To characterize the global failure of the target particle, in the first case the Christensen fracture criterion [40] is applied to the stress tensor globally averaged over the entire particle, assuming homogeneity of the material and ignoring stress variations within the particle. The second case considers random crack development due to the local tensile stress inside the particle under compression, and Weibull's weakest link theory [41] is applied to relate the fracture of the target particle to the standardized compression tests. The two criteria are not two calibrations of a single quantity. They interrogate the loaded particle at different scales, through different failure mechanisms, and with independent material inputs. Sections 2.4.1 and 2.4.2 define each in turn, and Section 2.4.3 describes how each is computed from the simulation output.

In both approaches, fracture is evaluated with two normalized failure criteria applied to the DEM output for the contact forces on, and the resulting stresses within, the target particle: the Christensen failure function f_C and the Weibull failure function f_W. Both are normalized so that the value one marks the onset of failure and values below one denote an intact particle, so that fracture is predicted when

$$f_C \geq 1 \qquad \text{or} \qquad f_W \geq 1, \tag{1}$$

where each criterion is evaluated and reported separately. Equation (1) states the failure condition of either function; it is not a combined criterion.

2.4.1 Christensen Criterion: Failure due to Globally Averaged Stress

The Christensen failure criterion is a relatively simple model for predicting both ductile and brittle failure in homogeneous, isotropic materials based on only two material parameters: the uniaxial tensile strength σ_T and the compressive strength σ_C of the material. The Christensen criterion [40] is a unified framework for the fracture of isotropic brittle materials due to compression, tension, and shear, with the failure function

$$f_C = \frac{1}{k_C^2}\left[\frac{a_C\, k_C}{\sqrt{3}}\,\sigma_{kk} + \frac{1+a_C}{2}\,s_{ij}s_{ij}\right], \tag{2}$$

where $\sigma_{kk} = \sigma_{xx}+\sigma_{yy}+\sigma_{zz}$ is the trace of the stress tensor $\bar{\boldsymbol{\sigma}}$ and is related to the hydrostatic pressure, $s_{ij} = \sigma_{ij} - \frac{1}{3}\sigma_{kk}\delta_{ij}$ is the deviatoric stress, and $s_{ij}s_{ij} = s_{xx}^2+s_{yy}^2+s_{zz}^2+2(s_{xy}^2+s_{xz}^2+s_{yz}^2)$ corresponds to the square of the effective shear stress. The two material parameters, a_C and k_C, are determined by requiring $f_C = 1$ at the two uniaxial failure states for compression and tension. Setting $f_C = 1$ at uniaxial compressive failure $\sigma_{xx} = -\sigma_C$, with all other stress components zero, gives

$$k_C = \frac{\sigma_C}{\sqrt{3}}, \tag{3}$$

and then setting $f_C = 1$ at uniaxial tensile failure $\sigma_{xx} = \sigma_T$, again with all other stress components zero, gives

$$a_C = \frac{\sigma_C}{\sigma_T} - 1. \tag{4}$$

We consider brittle materials here, where $\sigma_T < \sigma_C$, which yields $a_C > 0$. For the example of limestone used here, $\sigma_C = 147$ MPa [35] and $\sigma_T = 22.4$ MPa [35], so $a_C \approx 5.56$.

f_C is evaluated from the volume-averaged stress tensor of the target particle, and therefore describes the bulk response of the particle to the imposed stress state rather than any local field within it. The failure mechanism it encodes is a global critical state: failure occurs when the particle, taken as a whole, reaches a limiting combination of hydrostatic and deviatoric stress calibrated against the uniaxial compressive and tensile strengths of the material.

2.4.2 Weibull Criterion: Random Crack Development due to Compression-Induced Local Tensile Stress

For a more detailed consideration, a particle fractures under compression because of crack development inside it due to the compression-induced tensile stress [42]. Larger particles are more likely to contain more and larger random cracks, and therefore, break more easily. Correspondingly, in single particle crushing tests, a characteristic stress at failure σ_{pc} is defined as the failure load F_c normalized by the squared particle diameter [43, 44],

$$\sigma_{pc} \equiv \frac{F_c}{d_p^2}, \tag{5}$$

and the peak internal tensile stress driving fracture in diametral compression is proportional to F_c/d_p^2 through a geometry-dependent numerical factor of order one [42]. In these tests, σ_{pc} increases as the particle diameter d_p decreases [45–47], consistent with the expected dependence on the underlying flaw population.

Weibull's weakest-link statistics [41], initially proposed for the tensile strength of ceramics, can be ap-

plied to explain this size dependence [43], giving the scaling

$$\sigma_{pc}(d_p) = \sigma_{pc,0} \left(\frac{d_p}{d_0} \right)^{-3/m}, \tag{6}$$

where m is the Weibull modulus. Although $\sigma_{pc,0}$ is the stress at which particles with the reference diameter d_0 have a 37% probability of surviving the crush in the probabilistic model, for simplicity, we take $\sigma_{pc,0}$ as the crushing strength at which all the particles fracture. The Weibull modulus, the crushing strength and the reference diameter are taken from crushing-test experiments. For the example of a target particle made of limestone, the Weibull constants $m = 2.73$, $d_0 = 120\,\text{mm}$, and $\sigma_{pc,0} = 5.579\,\text{MPa}$ are taken from the particle crushing tests of Wang et al. [47].

Rearranging Equation (5) for the force and substituting the target particle diameter $d_p = 2r_t = 2r_g/R$ into Equation (6) gives the size-dependent critical force

$$F_c^{\mathsf{W}}(R) = \sigma_{pc}(d_p)\, d_p^2 = 4\,\sigma_{pc,0} \left(\frac{2r_g}{R d_0} \right)^{-3/m} \frac{r_g^2}{R^2}. \tag{7}$$

The Weibull failure function evaluates fracture directly from the contact forces, rather than by comparing a stress tensor with material properties, by referring them to F_c^{W}. The material input is the characteristic crushing stress measured experimentally in single-particle crushing tests for the material of interest, limestone in this case, although the approach can be used for any material provided that crush-test results are available.

The Weibull criterion acts at the scale of the flaw population inside the particle. It is evaluated from the contact forces transmitted through the particle and is compared with the crushing force measured in single-particle diametral compression. In that configuration the particle does not fail by compression itself: the compressive load generates a transverse tensile stress along the loading axis, and it is this compression-induced tension that splits the particle apart. The strength resisting it is set by the largest flaw the particle happens to contain, so it is governed by weakest-link statistics and depends on particle size. Mechanism, scale, and material input are therefore all distinct from those of Section 2.4.1.

2.4.3 Evaluation of the Criteria from the DEM Output

The two criteria are evaluated as f_C and f_W based on the resolved contact forces from DEM simulations. The Christensen function is computed from the per-particle stress tensor of the target particle, $\bar{\boldsymbol{\sigma}}$, in the size-bidisperse system, defined as [48, 49]:

$$\bar{\boldsymbol{\sigma}} \;=\; \frac{1}{V_t} \sum_i \mathbf{F}_i \otimes \boldsymbol{\ell}_i, \tag{8}$$

where $V_t = \frac{4}{3}\pi r_t^3$ is the target particle volume, $\otimes$ denotes the outer product, and $\mathbf{F}_i$ and $\boldsymbol{\ell}_i$ are the contact force and branch vector defined in Section 2.2. Equations (8) and (2) can be applied to both head-on and oblique collisions. LAMMPS reports the per-atom stress of the target particle from the per-atom virial [50, 51], which assigns to each contact i one half of the pair contribution,

$$\bar{\boldsymbol{\sigma}}_{\text{LAMMPS}} = \frac{1}{V_t} \sum_i \frac{1}{2}\, \mathbf{F}_i \otimes \mathbf{r}_i. \tag{9}$$

Here $\mathbf{r}_i$ is the center-to-center vector from the target particle to the grinding ball, of length $r_g + r_t$ and collinear with the branch vector $\boldsymbol{\ell}_i = -r_t\hat{\mathbf{n}}_i$, so that $\mathbf{r}_i = \frac{r_g+r_t}{r_t}\boldsymbol{\ell}_i$ and the two definitions differ only by the corresponding length ratio. The stress tensor used in Equation (8) is therefore obtained from the LAMMPS output by rescaling every component as

$$\bar{\boldsymbol{\sigma}} = \frac{2r_t}{r_g + r_t}\,\bar{\boldsymbol{\sigma}}_{\text{LAMMPS}} = \frac{2}{1+R}\,\bar{\boldsymbol{\sigma}}_{\text{LAMMPS}}. \tag{10}$$

This rescaled tensor is used when evaluating the failure function.

The Weibull function f_W is directly computed from the transmitted contact forces. A typical crushing test loads a particle diametrally between two platens, and trapped target particles are loaded analogously by the two grinding balls in Fig. 1 on head-on collisions. On oblique collisions, we assume that the analogous compression is in the direction of the unit vector $\hat{\mathbf{n}}_a$ connecting the two contact points.

With $F_{1,a}$ and $F_{2,a}$ the components of the two contact forces along $\hat{\mathbf{n}}_a$, taken positive in compression, the effective compression force is their average, floored at zero,

$$F_{\text{eff}} = \max\left(\frac{F_{1,a} + F_{2,a}}{2},\ 0\right). \tag{11}$$

The Weibull failure function is the ratio of the effective compression force to the critical force

$$f_W = \frac{F_{\text{eff}}}{F_c^{\text{W}}(R)}. \tag{12}$$

Each DEM run therefore produces two separate time series over the contact window: the per-particle stress tensor $\sigma_{ij}(t)$, from which $f_C(t)$ is evaluated through Equation (2), and the transmitted compression force $F_{\text{eff}}(t)$, from which $f_W(t)$ is evaluated through Equation (12). The maximum of each function over the contact window is recorded, and the collision is classified as fractured under a given criterion if that maximum reaches unity.

3 Model

This section develops the analytical model of the collision. In contrast to the numerical experiments of Section 2, the model requires no simulation input: given the initial configuration $(v, \alpha, \gamma, R, \mu)$, it predicts the outcome through three conditions evaluated in sequence. The incoming grinding ball must first reach the target particle (Section 3.1), the target particle must then be trapped between the two grinding balls rather than ejected (Section 3.2), and the impact velocity must finally exceed a critical value set by an energy perspective [52] (Section 3.4); the restitution coefficient e also enters the third condition, as a fixed material parameter of Table 1 rather than a collision variable. Section 3.5 collects the three conditions and Fig. 6 summarizes the decision sequence.

3.1 Impact Condition

Whether the incoming grinding ball can reach the target particle is determined solely by the opening angle $\alpha + \gamma$ and the size ratio, and contact with the target occurs before contact between the two

grinding balls only if

$$180^\circ - |\alpha + \gamma| \geq 2 \arcsin \frac{r_g}{r_g + r_t}, \tag{13}$$

or, equivalently, in terms of $R = r_g/r_t$

$$|\alpha + \gamma| \leq 2 \arccos \frac{R}{R+1}, \tag{14}$$

with the limit case shown in Fig. 3(a).

For larger openings, the fixed grinding ball blocks the trajectory, and the outcome is no contact between the incoming grinding ball and the target particle.

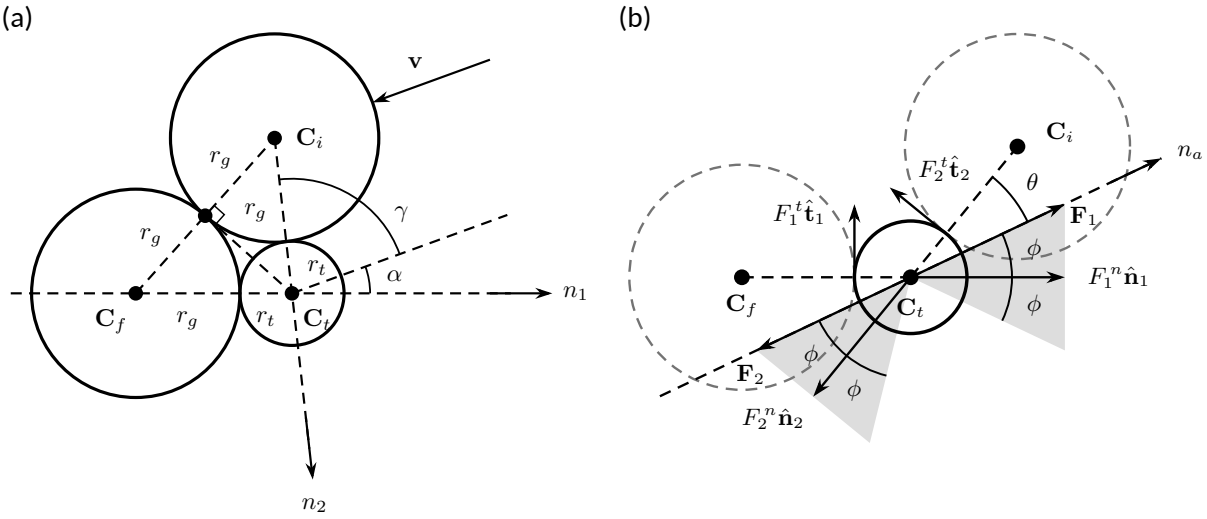


Figure 3: (a) Limiting impact geometry at which the incoming grinding ball (center $\mathbf{C}_i$, velocity $\mathbf{v}$) touches the fixed grinding ball ($\mathbf{C}_f$) and the target particle ($\mathbf{C}_t$) at the same instant, shown for $R = 2$. Dashed lines indicate construction lines: the n_1 and n_2 axes, the ray through $\mathbf{C}_t$ parallel to $\mathbf{v}$, and the lines of centers; the dot marks the contact point between the two grinding balls, and α and γ are measured at $\mathbf{C}_t$. (b) Free-body diagram of the target particle at the critical trapping case $\alpha + \gamma = 2\phi$. The contact forces are shown as normal components $F_i^n\hat{\mathbf{n}}_i$ and tangential components $F_i^t\hat{\mathbf{t}}_i$, with resultants $\mathbf{F}_i$; the shaded wedges are the Coulomb friction cones of half-angle $\phi = \arctan \mu$, and n_a is the common line of action of the two resultants. The grinding balls are drawn dashed.

3.2 Trapping Condition

Whether the target particle is trapped between the two grinding balls or ejected before it can be loaded is determined by the collision geometry and the friction coefficient. As shown in Fig. 3(b), the normal forces squeeze the target particle out, while the tangential forces keep it in, which is independent of the impact velocity.

The construction below generalizes the classical angle-of-nip condition of roll-crusher and high-pressure grinding-roll theory [27–30], in which a particle is captured only if the half-angle subtended at the two loading surfaces does not exceed the friction angle. The classical criterion assumes a symmetric geometry with a single nip half-angle. Here the two contact normals are not symmetric about the approach direction, so the condition involves two independent angles and emerges in the combination $\alpha + \gamma$; the symmetric roll geometry is recovered as the special case $\alpha = \gamma$.

The construction is summarized in Fig. 3(b). The target particle experiences a normal force from each

grinding ball, F_1^n along $\hat{\mathbf{n}}_1$ from the fixed grinding ball and F_2^n along $\hat{\mathbf{n}}_2$ from the incoming grinding ball, together with a tangential friction force F_i^t at each contact along $\hat{\mathbf{t}}_i = \hat{\mathbf{z}} \times \hat{\mathbf{n}}_i$. The resultant contact forces on the target particle are

$$\mathbf{F}_1 = F_1^n\,\hat{\mathbf{n}}_1 + F_1^t\,\hat{\mathbf{t}}_1, \qquad \mathbf{F}_2 = F_2^n\,\hat{\mathbf{n}}_2 + F_2^t\,\hat{\mathbf{t}}_2. \tag{15}$$

Coulomb's law requires $|F_i^t| \le \mu F_i^n$. Since $\mathbf{F}_i$ deviates from its contact normal by the angle $\arctan(|F_i^t|/F_i^n)$, each admissible resultant lies within a cone of half-angle

$$\phi = \arctan\mu \tag{16}$$

about its contact normal.

Since the inertia of the target particle is negligible compared with that of the grinding balls, the quasi-static condition can be applied to the target particle, leading to the force balance $\mathbf{F}_1 = -\mathbf{F}_2$. For the target particle to be held between the grinding balls rather than ejected sideways, the direction of $\mathbf{F}_1$ must lie within ϕ of $\hat{\mathbf{n}}_1$ and, because it must be the reverse of $\mathbf{F}_2$, within ϕ of $-\hat{\mathbf{n}}_2$. Since $\hat{\mathbf{n}}_1$ and $-\hat{\mathbf{n}}_2$ are separated by the angle $\alpha + \gamma$, this condition can be met only if

$$\frac{1}{2}|\alpha + \gamma| \le \phi = \arctan\mu. \tag{17}$$

The target particle is compressed under sustained double contact only if both frictional and geometric criteria are satisfied. Combining the frictional bound $|\alpha + \gamma| \le 2\arctan\mu$ with the impact condition of Equation (14) yields the trapping regime

$$|\alpha + \gamma| \le \min\left(2\arctan\mu,\ 2\arccos\frac{R}{R+1}\right). \tag{18}$$

3.3 Stress State of a Trapped Particle and Critical Contact Forces

When the target particle is held in sustained double contact as depicted in Sections 3.1 and 3.2, this section evaluates the Christensen criterion in terms of contact forces. Then the critical contact forces for both criteria can be used as the input to the energy perspective in Section 3.4.

As assumed in Section 3.2, since the inertia of the target particle is negligible compared with the grinding balls, the target particle is in quasi-static equilibrium with $\mathbf{F}_1 + \mathbf{F}_2 = 0$.

Let $\hat{\mathbf{n}}_a$ denote the unit vector along the line connecting both contact points, so the two forces are $\mathbf{F}_1 = F\,\hat{\mathbf{n}}_a$ and $\mathbf{F}_2 = -F\,\hat{\mathbf{n}}_a$. With the two contact points located at $\boldsymbol{\ell}_1 = -r_t\hat{\mathbf{n}}_1$ and $\boldsymbol{\ell}_2 = -r_t\hat{\mathbf{n}}_2$ from the target particle center, the separation of the two contact points is

$$\boldsymbol{\ell}_1 - \boldsymbol{\ell}_2 \;=\; -r_t\,(\hat{\mathbf{n}}_1 - \hat{\mathbf{n}}_2) \;=\; -\,2r_t\cos\theta\;\hat{\mathbf{n}}_a, \tag{19}$$

where θ is defined as the half-angle between $\hat{\mathbf{n}}_1$ and $-\hat{\mathbf{n}}_2$. Then Equation (8) becomes

$$\bar{\boldsymbol{\sigma}} \;=\; \frac{F\,\hat{\mathbf{n}}_a \otimes \boldsymbol{\ell}_1 - F\,\hat{\mathbf{n}}_a \otimes \boldsymbol{\ell}_2}{V_t} \;=\; \frac{F}{V_t}\,\hat{\mathbf{n}}_a \otimes (\boldsymbol{\ell}_1 - \boldsymbol{\ell}_2) \;=\; -\,\frac{2Fr\cos\theta}{V_t}\,\hat{\mathbf{n}}_a \otimes \hat{\mathbf{n}}_a. \tag{20}$$

In a frame aligned with $\hat{\mathbf{n}}_a$, the outer product $\hat{\mathbf{n}}_a \otimes \hat{\mathbf{n}}_a$ is simply $\mathrm{diag}(1,\,0,\,0)$, so

$$\bar{\boldsymbol{\sigma}} \;=\; \mathrm{diag}(-\sigma_0,\,0,\,0), \qquad \text{with} \quad \sigma_0 \;=\; \frac{2Fr\cos\theta}{V_t} \;=\; \frac{3F\cos\theta}{2\pi r_t^2}. \tag{21}$$

The trapped target particle is therefore equivalently under uniaxial compression along $\hat{\mathbf{n}}_a$ for every trapped geometry. For a head-on collision $\theta = 0$ and the uniaxial stress is a maximum; non-zero values of θ reduce the compressive stress attained at a given contact force. Writing the normal force at either contact as $F^n = F\cos\theta$, the uniaxial stress of Equation (21) becomes

$$\sigma_0 = \frac{2F^n r_t}{V_t} = \frac{3F^n}{2\pi r_t^2}. \tag{22}$$

The stress depends on the normal force alone, so it is the same for every trapped geometry at a given F^n.

For this uniaxial state, the invariants of Equation (2) are

$$\sigma_{kk} = -\sigma_0, \qquad s_{ij}s_{ij} = \tfrac{2}{3}\sigma_0^2, \tag{23}$$

and substituting them with k_C and a_C, as calibrated in Equations (3) and (4) as functions of material properties σ_C and σ_T, gives

$$f_C \;=\; 1 + \left(\frac{\sigma_0}{\sigma_C} - 1\right)\left(\frac{\sigma_0}{\sigma_T} + 1\right). \tag{24}$$

Since the second factor is always positive for $\sigma_0 \geq 0$, fracture ($f_C \geq 1$) is assumed to occur when $\sigma_0 \geq \sigma_C$. Setting $\sigma_0 = \sigma_C$ in Equation (22) yields the critical normal force

$$F_c^{\mathsf{C}} = \tfrac{2}{3}\pi r_t^2 \sigma_C. \tag{25}$$

The two thresholds are not referred to the same force component. The Christensen failure function is written in terms of the uniaxial stress $\sigma_0 = 2F^n r_t/V_t$, so its critical value F_c^{C} of Equation (25) is a threshold on the normal force at either contact for every trapped geometry. The Weibull failure function of Equation (12) is written in terms of the resultant along $\hat{\mathbf{n}}_a$ through Equation (11), so its critical value is the size-dependent crushing force $F_c^{\mathsf{W}}(R)$ of Equation (7).

3.4 Energy-Based Critical Velocity

The criteria in Section 2.4 evaluate fracture from DEM output, so every new parameter combination requires a full simulation. This section aims to analytically derive an equation that governs fracture, in which the critical impact velocity is expressed directly in terms of the material properties and the collision parameters following the energy perspective [52].

3.4.1 Head-On Critical Velocity

Consider first the simplest case, a head-on collision $\alpha = \gamma = 0^\circ$ with damping neglected, so the incident kinetic energy of the incoming grinding ball is stored entirely as elastic strain energy in the two contacts

at peak compression. The Hertz contact between two elastic spheres relates the normal force to the mutual overlap δ by

$$F^n(\delta) = \tfrac{4}{3}\, E^*\, R^{*1/2}\, \delta^{3/2}, \tag{26}$$

where the effective radius R^* and effective Young's modulus E^* are given by

$$\frac{1}{R^*} = \frac{1}{r_t} + \frac{1}{r_g} = \frac{1+R}{r_g}, \qquad \frac{1}{E^*} = \frac{1-\nu_t^2}{E_t} + \frac{1-\nu_g^2}{E_g}. \tag{27}$$

Each fracture criterion supplies a critical normal contact force F_c at which its failure function reaches unity; the criterion-specific forms are given at the end of this subsection. Setting $F^n = F_c$ and inverting Equation (26) gives the critical overlap

$$\delta_c = \left(\frac{3F_c}{4E^* R^{*1/2}}\right)^{2/3}, \tag{28}$$

and the elastic energy stored in a single contact at that overlap is

$$E_{\mathsf{el}} = \int_0^{\delta_c} F^n\, d\delta = \frac{8}{15}\, E^*\, R^{*1/2}\, \delta_c^{5/2} = \frac{8}{15}\left(\frac{3}{4}\right)^{5/3} E^{*-2/3}\, R^{*-1/3}\, F_c^{5/3}. \tag{29}$$

During a head-on collision, the target particle experiences the maximum force when all the initial kinetic energy is converted to the elastic energy stored at the two contacts. Equating $2E_{\mathsf{el}}$ to the initial kinetic energy of the incoming grinding ball, $\frac{1}{2}\,\rho_g\, V_g\, v_{c,0}^2$, gives the critical head-on velocity $v_{c,0}$,

$$v_{c,0}(R) = \frac{3^{5/6}}{2^{1/6}\sqrt{5\pi}}\,(1+R)^{1/6}\, r_g^{-5/3}\, \rho_g^{-1/2}\, E^{*-1/3}\, F_c^{5/6}. \tag{30}$$

where $V_g = \frac{4}{3}\pi r_g^3$ is the grinding ball volume and ρ_g its density.

The two criteria enter through the critical force F_c used in Equation (30). For the Christensen criterion it is F_c^{C} of Equation (25), with $r_t = r_g/R$. For the Weibull criterion, $F_c^{\mathsf{W}}(R)$ of Equation (7) is a threshold on the resultant force along $\hat{\mathbf{n}}_a$, so the corresponding critical normal force at either contact is $F_c^{\mathsf{W}}(R)\cos\theta$, with the head-on threshold recovered at $\theta = 0$. Substituting each criterion-specific critical normal force into Equation (30) gives the head-on thresholds $v_{c,0}^{\mathsf{C}}(R)$ and $v_{c,0}^{\mathsf{W}}(R)$ as functions of particle parameters, which are compared with the DEM fracture boundaries in Section 4.

3.4.2 Generalizing to All Geometries

In an oblique collision, only a fraction of the incident kinetic energy is converted into elastic potential energy at the contacts; the remainder stays as translational and rotational motion of the particles, and part of the stored energy sits in tangential rather than normal deformation. The energy–geometry factor G is the fraction of the incident kinetic energy that is delivered to normal compression of the two contacts at peak compression,

$$G(\alpha,\gamma) = \frac{2\kappa\,(\cos\alpha + \cos\gamma)^2}{\big[(\kappa+1) + (\kappa-1)\cos(\alpha+\gamma)\big]\big[9 - 5\cos(\alpha+\gamma)\big]}, \tag{31}$$

where κ is the Mindlin ratio of the tangential to the normal contact stiffness [26],

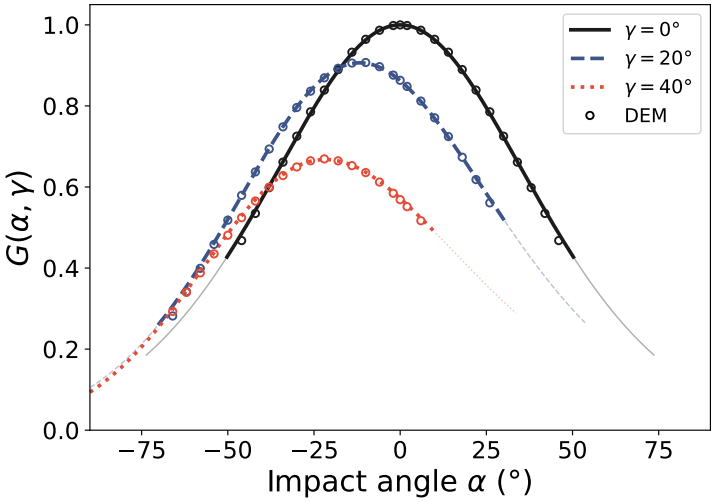


Figure 4: Energy–geometry factor $G(\alpha, \gamma)$ of Equation (31) with $\kappa = 0.68$, plotted against impact angle at $\gamma = 0°$, $20°$, and $40°$. Heavy segments lie inside the static trapping band of Equation (17) at $\mu = 0.47$; faded segments lie outside it, up to the reach limit of Equation (14) at $R = 4$. Open circles show the same factor measured from the DEM simulations, $G_{\mathrm{DEM}} = [v_c(0,0)/v_c(\alpha,\gamma)]^2$, obtained from the $f_C = 1$ threshold of v–α sweeps at each obliquity angle.

$$\kappa = \frac{3}{2\,(2-\nu)(1+\nu)} \approx 0.68, \tag{32}$$

with $\nu = \sqrt{\nu_t \nu_g}$ the mixed Poisson's ratio of Table 1.

The full derivation of Equation (31) is given in the Supplementary Information (Section S2, provided as a separate document). In a head-on collision $G(0,0) = 1$ for any κ, and G is symmetric in α and γ. Therefore, the energy balance becomes $G\,\frac{1}{2}\rho_g V_g v^2 = 2\,E_{\mathrm{el}}$, which generalizes the critical velocity for fracture to

$$v_c(\alpha, \gamma, R) = \frac{v_{c,0}(R)}{\sqrt{G(\alpha,\gamma)}}. \tag{33}$$

For the Weibull criterion, the critical normal force entering the energy balance is $F_c^{\mathrm{W}}(R)\cos\theta$, with $\theta = (\alpha+\gamma)/2$, so the geometry-dependent threshold becomes

$$v_c^{\mathrm{W}}(\alpha, \gamma, R) = \frac{v_{c,0}^{\mathrm{W}}(R)\,(\cos\theta)^{5/6}}{\sqrt{G(\alpha,\gamma)}}. \tag{34}$$

The factor $(\cos\theta)^{5/6}$ reaches one for head-on collisions and equals 0.92 at the trapping limit for $\mu = 0.47$, where $\theta = \arctan\mu$.

Fig. 4 plots G as a function of impact angle at three fixed obliquity angles, together with the same factor measured directly from the DEM simulations as $G_{\mathrm{DEM}} = [v_c(0,0)/v_c(\alpha,\gamma)]^2$ at $R = 4$. The measured points follow the analytic curves across all three obliquity angles. The factor equals one only for head-on impact and is symmetric under exchange of α and γ. For a positive obliquity angle the maximum of G shifts to negative impact angles, toward the configurations in which the two contact normals are least inclined to each other.

3.4.3 Accounting for Damping

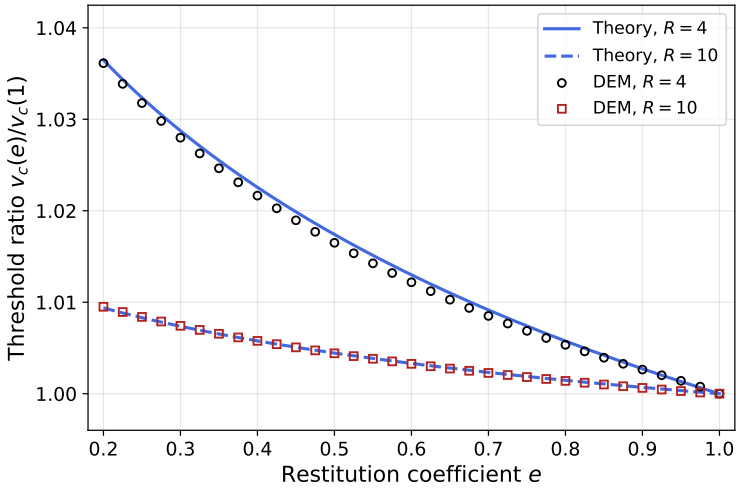


Figure 5: Validation of the damping factor using DEM simulations over 33 values of e spanning $[0.2, 1]$. Threshold ratio $v_c(e)/v_c(e{=}1)$ for head-on collisions ($\alpha = \gamma = 0°$) as a function of the restitution coefficient e. Solid and dashed curves are the predictions of Equation (39) at $R = 4$ and $R = 10$; open black circles and open red squares are the DEM-measured thresholds at $R = 4$ and $R = 10$, each normalized by its own lossless threshold.

The critical velocities above are derived from a lossless energy balance, while the DEM contact model dissipates energy in its dashpot, calibrated to the restitution coefficient e of Table 1. At equal impact speed, damping reduces the peak force transmitted through the trapped target particle by a factor $\Psi_{\text{trap}}(e, R)$, defined as the ratio of the damped to the lossless peak contact force. Its closed form, derived in the Supplementary Information (Section S3), is

$$\Psi_{\text{trap}}(e, R) = \left(1 + \lambda_{\text{trap}}^2\right)^{3/5} \exp\!\left(-\tfrac{6}{5}\lambda_{\text{trap}}\tau_{\text{pk}}\right) \left(\sin\tau_{\text{pk}}\right)^{1/5} \sin\!\left(\tau_{\text{pk}} + 2\arctan\lambda_{\text{trap}}\right), \tag{35}$$

where λ_{trap} is the damping index of the trapped compression mode and τ_{pk} is the phase at which the transmitted force peaks. The damping index is

$$\lambda_{\text{trap}} = \frac{\zeta_{\text{trap}}}{\sqrt{1 - \zeta_{\text{trap}}^2}}, \tag{36}$$

where ζ_{trap} is the effective damping ratio of the trapped compression mode, a function of the restitution coefficient and of the masses of the two bodies in contact,

$$\zeta_{\text{trap}} = \frac{-\ln e}{\sqrt{\pi^2 + (\ln e)^2}} \sqrt{\frac{m_t}{2\,(m_t + m_g)}}, \tag{37}$$

with $m_t = \frac{4}{3}\pi r_t^3 \rho_t$ the target particle mass and $m_g = \frac{4}{3}\pi r_g^3 \rho_g$ the grinding ball mass. The size ratio enters through the mass ratio, $m_t/m_g = (\rho_t/\rho_g)\, R^{-3}$, with ρ_t and ρ_g the densities of Table 1. The phase τ_{pk} is the unique root of

$$\tfrac{1}{5}\cot\tau_{\text{pk}} + \cot\!\left(\tau_{\text{pk}} + 2\arctan\lambda_{\text{trap}}\right) = \tfrac{6}{5}\,\lambda_{\text{trap}}, \qquad 0 < \tau_{\text{pk}} < \pi - 2\arctan\lambda_{\text{trap}}, \tag{38}$$

solved numerically. Because fracture is a force threshold and the lossless peak force scales as $v^{6/5}$ ac-

cording to Equation (30), a force deficit of Ψ_{trap} converts into a velocity increase of $\Psi_{\text{trap}}^{-5/6}$, and the critical velocities including both geometry and damping take their final forms, for the Christensen and Weibull criteria respectively,

$$v_c^{\mathsf{C}}(\alpha, \gamma, R, e) = \Psi_{\text{trap}}^{-5/6}(e, R)\, \frac{v_{c,0}^{\mathsf{C}}(R)}{\sqrt{G(\alpha, \gamma)}}, \tag{39}$$

$$v_c^{\mathsf{W}}(\alpha, \gamma, R, e) = \Psi_{\text{trap}}^{-5/6}(e, R)\, \frac{v_{c,0}^{\mathsf{W}}(R)\, (\cos\theta)^{5/6}}{\sqrt{G(\alpha, \gamma)}}. \tag{40}$$

The prediction of Equation (35) follows the DEM-measured fracture thresholds closely for restitution from 0.2 to 1, as shown in Fig. 5. At the production values $e = 0.5$ and $R = 4$, $\Psi_{\text{trap}} = 0.979$, so damping raises the head-on fracture threshold by 1.7%, and the critical velocities used throughout Section 4 are those of Equations (39) and (40) evaluated at the restitution coefficient of Table 1.

Further corrections to the critical velocity are not included. The material strengths entering both criteria are quasi-static values, whereas the contacts simulated here last 10–100 μs, corresponding to strain rates of order 10^2–10^3 s^{-1}, where brittle rock stiffens appreciably. A rate-stiffened material would raise both critical forces, and both criteria would therefore over-predict fracture near threshold. The Weibull constants are additionally extrapolated well below the size range in which they were measured, with an exponent $3/m > 1$ that makes the extrapolation super-linear in size ratio. These are strength-side corrections rather than energy-side ones, but they act on the same threshold and in the same direction as the damping correction.

3.5 Model Summary

The model reduces the outcome of a collision to three conditions evaluated in sequence from the initial configuration $(v, \alpha, \gamma, R, \mu)$, with the restitution coefficient e entering as a fixed material parameter. First, impact: the incoming grinding ball reaches the target particle only if $|\alpha + \gamma| \leq 2 \arccos[R/(R + 1)]$, Equation (14). Second, trapping: the target particle is held between the two grinding balls only if $|\alpha + \gamma| \leq 2 \arctan \mu$, Equation (17). Third, fracture: a trapped target particle breaks only if the impact velocity exceeds the critical velocity $v_c(\alpha, \gamma, R, e)$ of Equation (39), for the Weibull criterion with the factor of Equation (40). A collision that fails the first condition leaves the target particle untouched; one that fails the second ejects the target particle intact; one that fails the third loads the target particle without breaking it. The decision sequence is summarized in Fig. 6.

4 Results and Discussion

4.1 Effect of Collision Geometry on Fracture

The effect of collision geometry on fracture is examined with three fracture maps in Fig. 7 using the same color coding as in Fig. 6: black for no contact, green for an intact target particle, and red for fracture. Panels (a)–(c) show the v–α map at $\gamma = 0°$, the v–γ map at $\alpha = 0°$, and the α–γ map at $v = 3$ m/s, respectively. For a head-on collision, the fracture threshold predicted by the DEM lies between 2.5 and 2.6 m/s, consistent with the analytic prediction of Equation (39), $v_c^{\mathsf{C}} = 2.52$ m/s. As

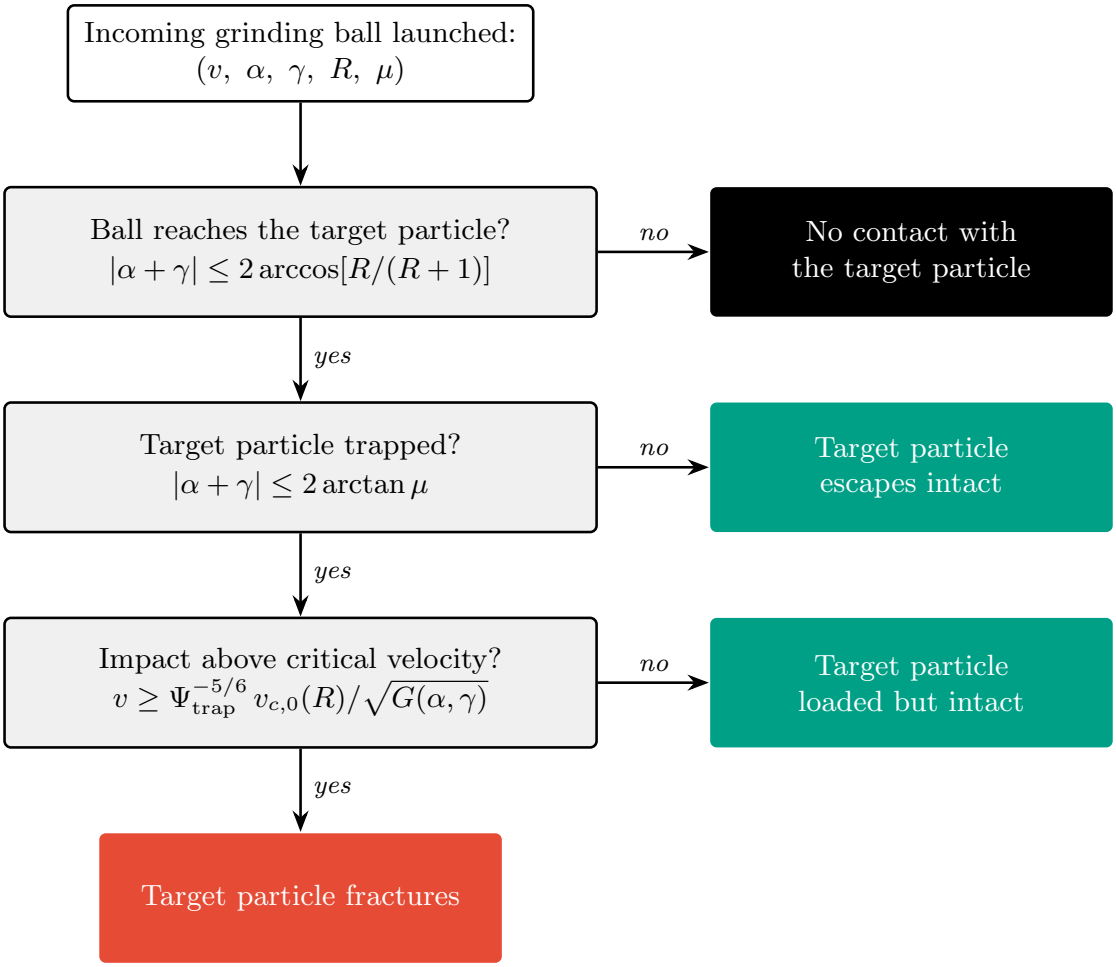


Figure 6: Decision sequence of the collision model. Each collision is classified by three conditions evaluated in order: the impact condition of Equation (14), the trapping condition of Equation (17), and the critical-velocity condition of Equation (39), with the Weibull criterion using the threshold of Equation (40). Outcome colors match the fracture maps: black denotes no contact, green an intact target particle, and red fracture.

the impact angle increases, the threshold rises, and across the trapped window the dashed prediction $v_c = \Psi_{\text{trap}}^{-5/6}\, v_{c,0}/\sqrt{G(\alpha,\gamma)}$ of Equation (39) follows the $f_C = 1$ contour line from the DEM simulations closely, indicating that the energy–geometry factor G controls the variation of the velocity threshold away from head-on impact.

The v–γ fracture map at $\alpha = 0°$ in Fig. 7(b) is nearly identical to the v–α map of panel (a): the threshold rises from the same head-on value as the obliquity angle grows, and it is truncated by the same trapping cutoff. The model explains this coincidence: $G(\alpha,\gamma)$ is symmetric under exchange of its two angles, so the two single-angle maps probe the same factor, $G(\alpha,0) = G(0,\alpha)$.

The α–γ fracture map in Fig. 7(c) shows the two geometry parameters acting together at fixed velocity. The fractured region is not centered on $\alpha = 0$: at a fixed obliquity angle it extends farther toward negative impact angles, following the configurations in which the two contact normals stay least inclined to each other, and its boundary again follows the threshold contour line of Equation (39) closely.

The interior trend is interrupted sharply at the trapping boundary of Equation (17), which appears as a horizontal truncation at $\alpha \approx \pm 50.4°$ in panel (a), as the cutoff at $\gamma \approx 50.4°$ in panel (b), and as the

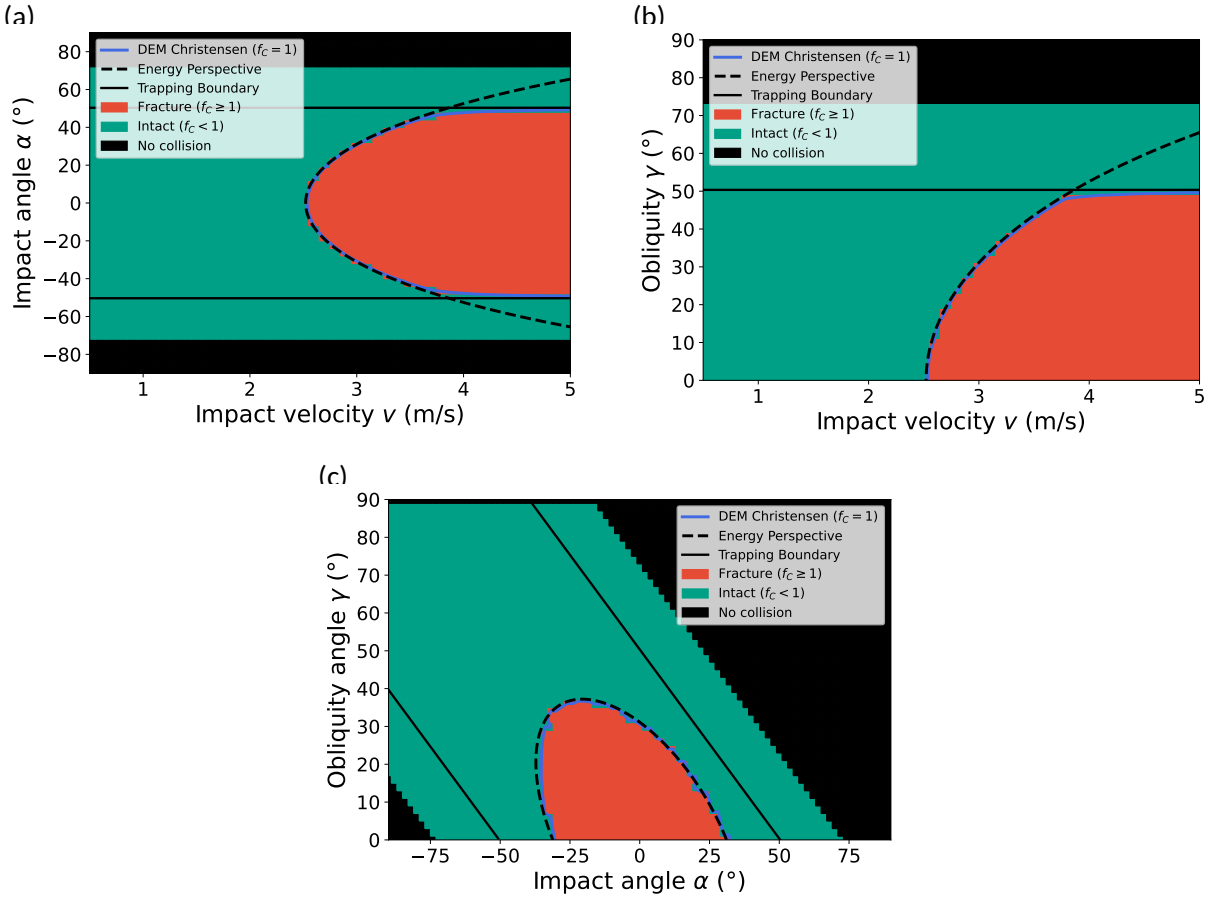


Figure 7: DEM fracture maps for the Christensen criterion. (a) v–α fracture map at $\gamma = 0°$. (b) v–γ fracture map at $\alpha = 0°$. (c) α–γ fracture map at $v = 3$ m/s. All maps are at $R = 4$ and $\mu = 0.47$. Red denotes predicted fracture ($f_C \geq 1$), green denotes intact collisions ($f_C < 1$), and black denotes configurations with no collision, beyond the reach limit of Equation (14). The solid blue curve is the $f_C = 1$ contour line based on DEM, the solid black lines are the static trapping boundary of Equation (17), and the dashed black curve is the analytical prediction of Equation (39) based on the energy perspective.

diagonal band in panel (c). Because the trapping condition is purely geometric, this cutoff is independent of v: beyond it, no fracture occurs at any simulated velocity up to 5 m/s.

Beyond the trapped window, the maps also exhibit the reach limit of Equation (14): no collision occurs beyond $|\alpha + \gamma| \approx 73.7°$ at $R = 4$, visible as the black corners of panel (c). In a mill, collisions can be steered into the trapped window by operating at subcritical rotation speeds that favor cascading motion [53] and by lifter and liner designs that promote direct, near-head-on impacts [32], so that the energy threshold, rather than ejection, decides the outcome.

4.2 Effect of Friction

The effect of friction is examined in Fig. 8, the μ–α fracture map at $v = 3$ m/s, $\gamma = 0$. The fracture wedge opens outward with increasing μ following the trapping boundary $\alpha_c = \pm 2 \arctan \mu$ corresponding to Equation (17), and the DEM contour line follows this opening closely for $\mu \lesssim 0.3$. Beyond that, the wedge saturates at $|\alpha| \approx 31°$ in the DEM, compared with $31.1°$ as predicted by Equation (39).

Friction therefore acts on fracture only through the trapping condition: it decides whether the target particle is held between the two grinding balls, not how hard the particle must be struck. Consistent

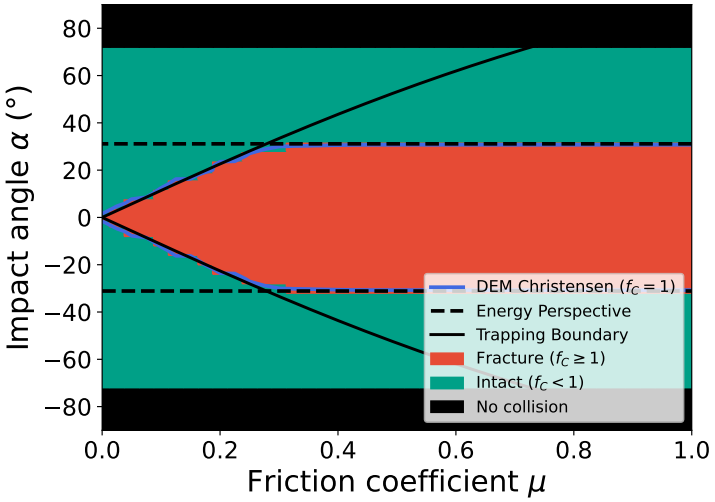


Figure 8: μ–α fracture map for the Christensen criterion at $v = 3$ m/s, $\gamma = 0°$, $R = 4$. Red denotes predicted fracture ($f_C \geq 1$), green denotes intact collisions ($f_C < 1$), and black denotes configurations with no collision, beyond the reach limit of Equation (14). The solid blue curve is the $f_C = 1$ contour line based on DEM, the solid black lines are the static trapping boundary of Equation (17), and the dashed black curve is the analytical prediction of Equation (39) based on the energy perspective.

with this, at fixed geometry ($\alpha = -20°$, $\gamma = 0$) the DEM threshold velocity varies by less than 0.2% across $\mu = 0.2$–1.0, as expected for sticking contacts, for which the friction coefficient never enters the energy factor of Equation (31). In operation, the effective friction coefficient can be tuned through the surface roughness of the grinding media, coatings, or, in wet grinding, the chemistry of the slurry and its additives [54]. The saturation of the wedge implies that moderate friction suffices: raising μ beyond about 0.3 no longer expands the fractured region, while over-lubrication that shrinks the trapping window should be avoided [55].

4.3 Effect of Size Ratio

The size ratio R influences both the reach limit and the head-on critical velocity.

The effect of size ratio on the head-on critical velocity v_c is examined in Fig. 9. v_c decreases with increasing R for both fracture criteria. Finer target particles are easier to fracture because the stress is more concentrated.

In milling terms, finer target particles are easier to break once trapped but harder to confine, because the reach limit of Equation (14) narrows as R grows. In practice, fracture probability is maximized by keeping a balanced ball mix, with large balls for coarse ore and small balls for fine ore [56, 57], and by continuously removing fine particles through classification [58, 59].

4.4 Comparison of Christensen and Weibull Predictions

Different criteria provide different dependence of v_c on R. The Christensen threshold

falls steeply, from 2.52 m/s at $R = 4$ to approximately 0.3 m/s at $R = 16$, while the Weibull threshold declines more shallowly, because the Weibull size effect makes smaller particles statistically stronger ($\sigma_{pc} \propto d_p^{-3/m}$) and partially offsets the geometric weakening. Both trends are confirmed by the DEM

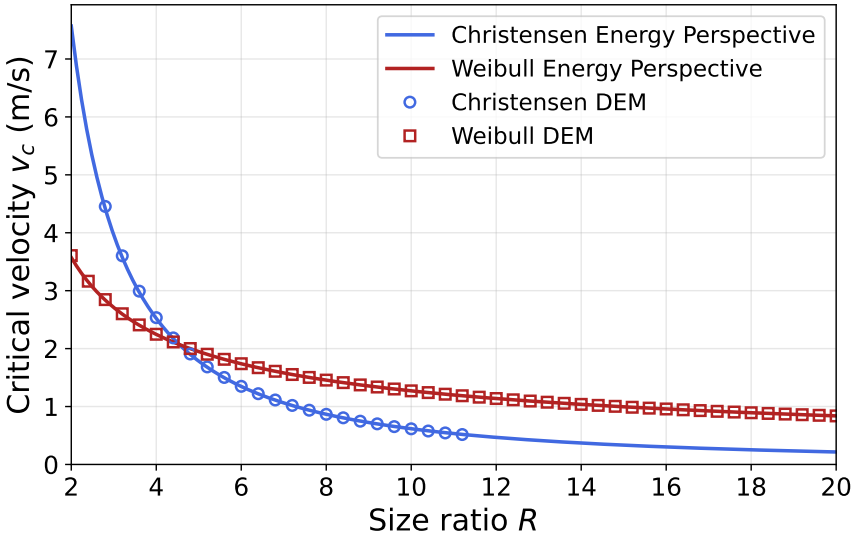


Figure 9: Analytic head-on ($\alpha = \gamma = 0$) critical velocity v_c of Equations (39) and (40) as a function of size ratio $R = r_g/r_t$, evaluated at $e = 0.5$ with the Christensen criterion (blue) and the Weibull criterion (red). Open blue circles and open red squares mark the corresponding criteria applied to forces resolved in DEM, the first upward $f = 1$ crossing along v in the v–R sweep at $\alpha = \gamma = 0°$ and $\mu = 0.47$. The grinding ball radius $r_g = 25$ mm is held fixed, and the target particle radius r_t is varied.

thresholds measured along the v–R sweep, which follow their respective analytic curves across the full size ratio range. With the production calibration ($d_0 = 120$ mm), the two curves cross at $R = 4.54$: below the crossing, the Weibull criterion predicts easier fracture than the Christensen criterion, and above it the order reverses.

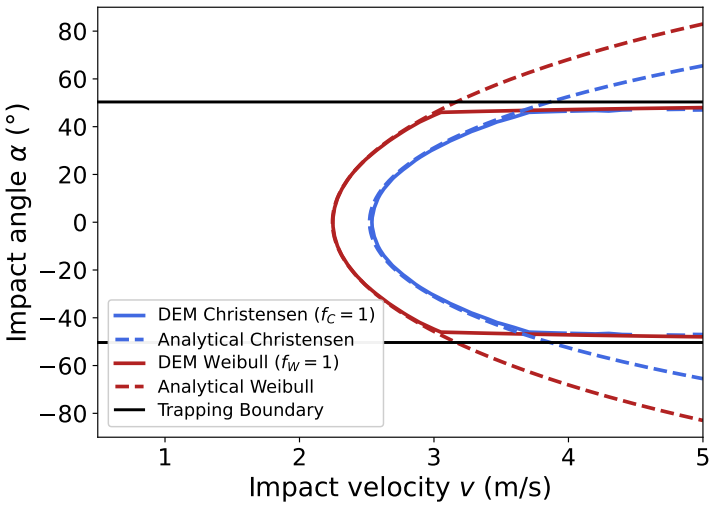


Figure 10: Christensen and Weibull fracture thresholds in the v–α plane at $\gamma = 0°$, $R = 4$, $\mu = 0.47$. Solid curves are the $f = 1$ contour lines based on DEM and dashed curves are the analytical predictions of Equation (39) for the Christensen criterion and Equation (40) for the Weibull criterion, each evaluated with its own criterion's $v_{c,0}$, in blue for the Christensen criterion and red for the Weibull criterion; the solid black lines are the static trapping boundary of Equation (17).

Fig. 10 compares the Christensen and Weibull predictions by overlaying their fracture contour lines in the v–α plane. The Weibull threshold sits lower in head-on impact: the DEM transition occurs between 2.2 and 2.3 m/s for f_W, compared with 2.5–2.6 m/s for f_C, consistent with the analytic values of Equa-

tions (40) and (39), $v_c^{\mathsf{W}} = 2.25$ m/s and $v_c^{\mathsf{C}} = 2.52$ m/s at $R = 4$, a difference of about 11%. Away from head-on impact, the two criteria no longer differ only by this constant offset: the Weibull contour drops relatively as $|\alpha|$ grows, following the additional geometric factor $(\cos\theta)^{5/6}$ in Equation (40) with $\theta = (\alpha+\gamma)/2$, which lowers v_c^{W} by about 8% at the static trapping limit for $\mu = 0.47$. In both cases the remaining angle dependence follows the energy transfer through $G(\alpha,\gamma)$, so each dashed curve tracks the DEM contour of its own criterion. The residual offset between the two thresholds comes from the head-on calibration: f_C is fixed by the compressive strength σ_C through F_c^{C}, while f_W is fixed by the size-dependent crushing force of the Weibull statistics through $F_c^{\mathsf{W}}(R)$.

4.5 Further Validation of the Analytical Model

Defining the criterion-specific effective velocities,

$$v_{\mathsf{eff}}^{\mathsf{C}} = v\sqrt{G(\alpha,\gamma)}, \qquad v_{\mathsf{eff}}^{\mathsf{W}} = v\sqrt{G(\alpha,\gamma)}\,(\cos\theta)^{-5/6}, \tag{41}$$

with $\theta = (\alpha+\gamma)/2$, the fracture conditions of Equations (39) and (40) can each be rearranged into a single comparison: fracture is predicted when

$$v_{\mathsf{eff}}(v,\alpha,\gamma) \geq \Psi_{\mathsf{trap}}^{-5/6}(e,R)\, v_{c,0}(R). \tag{42}$$

The left side is the load: it contains only the kinematics of the incoming grinding ball, through the impact velocity v, and the collision geometry through $G(\alpha,\gamma)$ for both criteria and, for the Weibull criterion, additionally through θ. The right side is the resistance: it contains the strength and size of the target particle, through the material properties and the size ratio entering the head-on critical velocity $v_{c,0}(R)$, and through the damping factor $\Psi_{\mathsf{trap}}^{-5/6}(e,R)$ of Equation (35), which depends on the restitution coefficient and the size ratio. Fracture is predicted when the load reaches the resistance, so in the $(v_{\mathsf{eff}},\ \Psi_{\mathsf{trap}}^{-5/6} v_{c,0})$ plane the predicted fracture boundary is the diagonal line $v_{\mathsf{eff}} = \Psi_{\mathsf{trap}}^{-5/6} v_{c,0}$.

This comparison applies only to collisions in which the target particle is actually compressed between the two grinding balls, so the test set is a sweep of $300{,}000$ DEM runs with the five parameters drawn uniformly at random over the ranges of Section 2 (with $\mu \geq 0.05$), restricted at generation to the trapped neighborhood: configurations were accepted only if $|\alpha+\gamma|$ lies within the frictional trapping band extended by a 2° margin beyond the static boundary of Equation (17), and inside the reach limit of Equation (14). The margin deliberately probes the ejection transition: $293{,}700$ runs (97.9%) satisfy the trapping regime of Equation (18) exactly, and the remaining $6{,}300$, which lie in the margin outside the friction cones, experience no sustained compression and are excluded from the scatter plot. Each retained run is plotted in Fig. 11 by its load v_{eff} and resistance $v_{c,0}$. The diagonal threshold of Equation (42) classifies the DEM outcome correctly in 99.43% of the trapped runs for the Christensen criterion and 99.29% for the Weibull criterion: the analytic energy theory reproduces the simulated fracture outcome across the full five-parameter domain, reducing the fracture condition to one comparison between a load from kinematics and a material resistance.

The error structure is one-sided for both criteria. For the Christensen criterion, essentially every misclassified run is one in which the threshold predicts fracture while the simulated particle stays intact ($1{,}660$ such runs, versus 2 missed fractures). For the Weibull criterion the same pattern holds, with $1{,}968$ runs

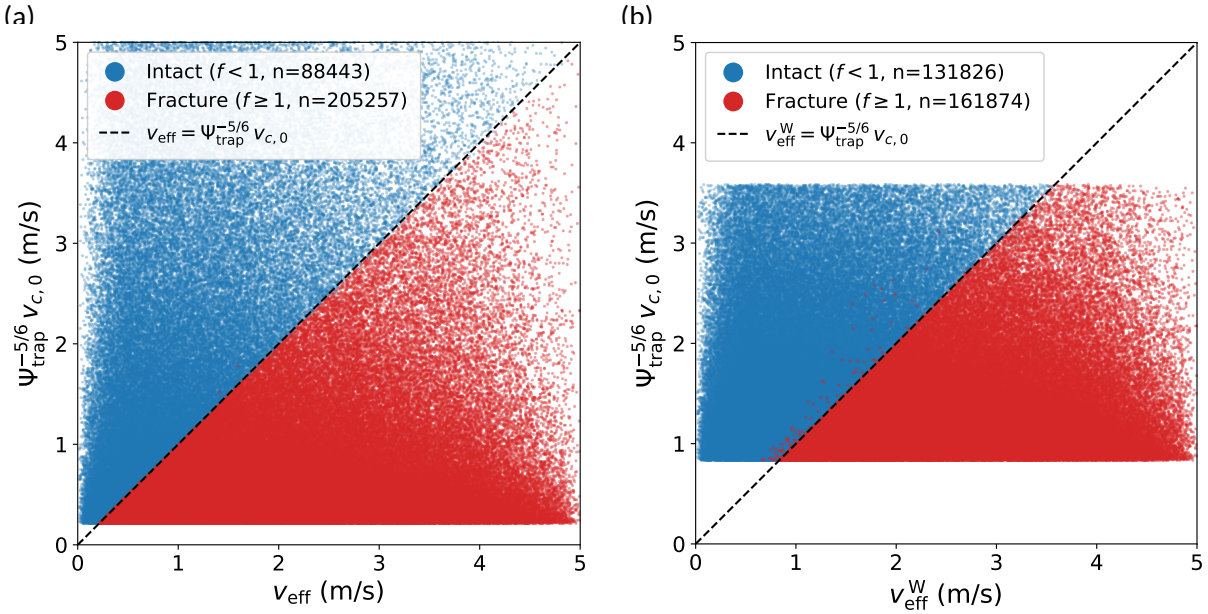


Figure 11: Every trapped run from the random sweep of $300{,}000$ collisions described in the text, plotted by its effective velocity against the head-on critical velocity $\Psi_{\text{trap}}^{-5/6}(e, R)\, v_{c,0}(R)$, for (a) the Christensen criterion using $v_{\text{eff}}^{\text{C}} = v\sqrt{G(\alpha,\gamma)}$ and (b) the Weibull criterion using $v_{\text{eff}}^{\text{W}} = v\sqrt{G(\alpha,\gamma)}(\cos\theta)^{-5/6}$. Blue points are intact outcomes ($f < 1$) and red points are fractured outcomes ($f \geq 1$); the dashed diagonal is the reduced fracture threshold $v_{\text{eff}} = \Psi_{\text{trap}}^{-5/6}\, v_{c,0}$ of Equation (42). Both panels share the frame 0–5 m/s; in (a), the $12{,}084$ runs with $\Psi_{\text{trap}}^{-5/6}\, v_{c,0} > 5$ m/s (4.1%, all intact) lie above the frame.

predicted to fracture that stay intact in the DEM, versus 120 missed fractures. The energy law therefore acts as a conservative predictor under both criteria.

The same sweep also quantifies how the two criteria compare with each other. When the trapped runs are sorted from most to least damaging, once by the value of f_C and once by the value of f_W, the two orderings nearly coincide: the Spearman rank correlation between them is 0.90, where a value of one corresponds to identical orderings. The two criteria therefore agree on which collisions are the most damaging, even though they are evaluated from different DEM outputs, and they differ mainly in where the fracture threshold is placed.

The misclassified runs concentrate in two situations. First, the large majority of the false-fracture outliers, runs predicted to fracture that stay intact in the DEM, lie within 5% of the fracture threshold and about half within 2%, corresponding to marginal collisions in which the predicted load exceeds the resistance by only a few percent. Second, a smaller share of the outliers lie within 2° of the static trapping boundary, where a configuration that is trapped statically can still slip out of the friction cones before the contact forces reach their maximum, so the target particle is ejected before full compression develops; the extreme false-fracture outliers, in which the predicted load exceeds the resistance by more than 20%, sit almost entirely on that boundary (median distance 0.2°). In practice, the comparison of Equation (42) serves as a near-complete, conservative descriptor of fracture across the trapped domain, with deviations confined to the near-threshold band and the trapping-boundary fringe.

5 Conclusions

This study combined DEM simulations, two independent fracture criteria, and analytic contact geometry to connect three-body collision mechanics to ore fracture in ball milling. A target particle initially placed between a fixed and an incoming grinding ball was simulated over wide ranges of impact velocity, impact angle, obliquity angle, size ratio, and friction coefficient, and each collision was evaluated with a stress-based Christensen criterion and a force-based Weibull criterion. Across this parameter space, two governing fracture mechanisms emerged and were captured by closed-form boundaries: a geometry-limiting regime, in which friction and collision orientation decide whether the target particle is trapped at all, and a velocity-limiting regime, in which the energy delivered to compression decides whether a trapped particle breaks.

For fixed sizes and friction, the most effective fracture occurs in head-on collisions at sufficiently high velocity. Within the trapped window the critical velocity is lowest for head-on impacts and rises as the collision angles grow; outside the window, the collision is glancing, the particle is ejected, and the outcome becomes independent of velocity. Finer particles fracture more easily once trapped but are less likely to remain confined, and friction mainly determines the width of the trapped window while having a much weaker effect on the load inside it. Across $300{,}000$ randomized collisions, the comparison of the effective impact velocity against the critical velocity classified the simulated outcome correctly in 99% of trapped collisions for both criteria, reducing a five-parameter fracture condition to a single equation. The remaining errors are conservative for both criteria and concentrate where the model idealizations are most strained: within a few percent of the fracture threshold, and at the fringe of the trapping window, where the particle slips out before compression peaks.

In practice, fracture probability is raised by steering collision kinematics toward near-head-on, low-offset impacts and by managing the size distribution of the charge. The former can be achieved by operating at sub-critical rotation speeds that promote cascading and by lifter and liner designs that favor direct impacts; the latter by keeping a balanced ball mix and continuously removing fine particles through classification. The friction that holds the trapping window open can be tuned through the surface condition of the grinding media or, in wet grinding, the chemistry of the slurry and its additives. Since the window gains little beyond moderate friction, over-lubrication that shrinks the trapping domain is the main condition to avoid.

The next step of this investigation is to simulate a realistic mill slice with lifters, sub-critical speed, and representative fill, and to extract the joint distribution of impact conditions experienced by the ore particles. Convolving that distribution with the fracture maps developed here would yield mill-scale predictions of how often particles are trapped and squeezed, and of the aggregate breakage probability at a given operating point. A particle replacement model can then be embedded, in which a particle satisfying the fracture criterion is replaced by daughter fragments sampled from a measured breakage function, connecting the single-collision physics established here to measured size-reduction trajectories. Grinding consumes a large share of industrial energy while less than 1% of the energy input to comminution creates new surface area; identifying the collisions that actually break ore is the first step toward spending that energy more selectively.

References

[1] A.-Z. M. Abouzeid, D. W. Fuerstenau, Grinding of mineral mixtures in high-pressure grinding rolls, International Journal of Mineral Processing 93 (1) (2009) 59–65.

[2] N. A. Aydoğan, L. Ergün, H. Benzer, High pressure grinding rolls (HPGR) applications in the cement industry, Minerals Engineering 19 (2) (2006) 130–139.

[3] S. Malkin, T. Hwang, Grinding mechanisms for ceramics, CIRP Annals 45 (2) (1996) 569–580.

[4] W. Gao, F. Chen, X. Wang, Q. Meng, Recent advances in processing food powders by using superfine grinding techniques: A review, Comprehensive Reviews in Food Science and Food Safety 19 (4) (2020) 2222–2255.

[5] M. Nakach, J.-R. Authelin, A. Chamayou, J. Dodds, Comparison of various milling technologies for grinding pharmaceutical powders, International Journal of Mineral Processing 74 (2004) S173–S181.

[6] B. Ji, W. Zhang, The effect of mechanical grinding and thermal treatment on the recovery of rare earth elements (REEs) from kaolinite, Powder Technology 394 (2021) 622–631.

[7] L. M. Tavares, A review of advanced ball mill modelling, KONA Powder and Particle Journal 34 (2017) 106–124.

[8] J. Jeswiet, A. Szekeres, Energy consumption in mining comminution, Procedia CIRP 48 (2016) 140–145.

[9] G. Ballantyne, M. Powell, Benchmarking comminution energy consumption for the processing of copper and gold ores, Minerals Engineering 65 (2014) 109–114.

[10] D. Fuerstenau, A.-Z. Abouzeid, The energy efficiency of ball milling in comminution, International Journal of Mineral Processing 67 (1-4) (2002) 161–185.

[11] S. Alvarado, J. Algüerno, H. Auracher, A. Casali, Energy–exergy optimization of comminution, Energy 23 (2) (1998) 153–158.

[12] Z.-X. Zhang, F. Ouchterlony, Energy requirement for rock breakage in laboratory experiments and engineering operations: A review, Rock Mechanics and Rock Engineering 55 (2) (2022) 629–667.

[13] O. E. Ige, D. V. Von Kallon, D. Desai, Carbon emissions mitigation methods for cement industry using a systems dynamics model, Clean Technologies and Environmental Policy 26 (3) (2024) 579–597.

[14] T. Norgate, N. Haque, Energy and greenhouse gas impacts of mining and mineral processing operations, Journal of Cleaner Production 18 (3) (2010) 266–274.

[15] S. Kittipongvises, Assessment of environmental impacts of limestone quarrying operations in Thailand, Rigas Tehniskas Universitates Zinatniskie Raksti 20 (1) (2017) 67–83.

[16] L. Tavares, R. King, Single-particle fracture under impact loading, International Journal of Mineral Processing 54 (1) (1998) 1–28.

[17] O. Genc, L. Ergün, H. Benzer, Single particle impact breakage characterization of materials by drop weight testing, Fizykochemiczne Problemy Mineralurgii/Physicochemical Problems of Mineral Processing 38 (2004) 241–255.

[18] A. S. Erdem, Ş. L. Ergün, The effect of ball size on breakage rate parameter in a pilot scale ball mill, Minerals Engineering 22 (7-8) (2009) 660–664.

[19] D. Ramkrishna, The status of population balances, Reviews in Chemical Engineering 3 (1) (1985) 49–95.

[20] Y. Duan, P. B. Umbanhowar, J. M. Ottino, R. M. Lueptow, Modelling segregation of bidisperse granular mixtures varying simultaneously in size and density for free surface flows, Journal of Fluid Mechanics 918 (2021) A20.

[21] S. Gao, J. M. Ottino, P. B. Umbanhowar, R. M. Lueptow, Modeling granular segregation for overlapping species distributions, Chemical Engineering Science 231 (2021) 116259.

[22] H. Xiao, P. B. Umbanhowar, J. M. Ottino, R. M. Lueptow, Modelling density segregation in flowing bidisperse granular materials, Proceedings of the Royal Society A: Mathematical, Physical and Engineering Sciences 472 (2191) (2016) 20150856.

[23] S. Gao, J. M. Ottino, P. B. Umbanhowar, R. M. Lueptow, Percolation of a fine particle in static granular beds, Physical Review E 107 (1) (2023) 014903.

[24] S. Gao, J. M. Ottino, R. M. Lueptow, P. B. Umbanhowar, Vertical velocity of a small sphere in a sheared granular bed, Physical Review Research 6 (2) (2024) L022015.

[25] S. Luding, Cohesive, frictional powders: contact models for tension, Granular Matter 10 (4) (2008) 235–246.

[26] R. D. Mindlin, Compliance of elastic bodies in contact, Journal of Applied Mechanics 16 (3) (1949) 259–268.

[27] J. R. Johanson, A rolling theory for granular solids, Journal of Applied Mechanics 32 (4) (1965) 842–848. arXiv:https://asmedigitalcollection.asme.org/appliedmechanics/article-pdf/32/4/842/5447239/842_1.pdf, doi:10.1115/1.3627325.
URL https://doi.org/10.1115/1.3627325

[28] G. Bindhumadhavan, J. Seville, M. Adams, R. Greenwood, S. Fitzpatrick, Roll compaction of a pharmaceutical excipient: Experimental validation of rolling theory for granular solids, Chemical Engineering Science 60 (14) (2005) 3891–3897.

[29] K. A. Yehia, Estimation of roll press design parameters based on the assessment of a particular nip region, Powder Technology 177 (3) (2007) 148–153.

[30] P. Kleinebudde, Improving process understanding in roll compaction, Journal of Pharmaceutical Sciences 111 (2) (2022) 552–558.

[31] A. Datta, R. K. Rajamani, A direct approach of modeling batch grinding in ball mills using population balance principles and impact energy distribution, International Journal of Mineral Processing 64 (4) (2002) 181–200.

[32] P. W. Cleary, Charge behaviour and power consumption in ball mills: sensitivity to mill operating conditions, liner geometry and charge composition, International Journal of Mineral Processing 63 (2) (2001) 79–114.

[33] A. P. Thompson, H. M. Aktulga, R. Berger, D. S. Bolintineanu, W. M. Brown, P. S. Crozier, P. J. In't Veld, A. Kohlmeyer, S. G. Moore, T. D. Nguyen, et al., LAMMPS-a flexible simulation tool for particle-based materials modeling at the atomic, meso, and continuum scales, Computer Physics Communications 271 (2022) 108171.

[34] D. Antypov, J. Elliott, On an analytical solution for the damped Hertzian spring, EPL (Europhysics Letters) 94 (5) (2011) 50004.

[35] S. Grange, P. Forquin, S. Mencacci, F. Hild, On the dynamic fragmentation of two limestones using edge-on impact tests, International Journal of Impact Engineering 35 (9) (2008) 977–991. doi:10.1016/j.ijimpeng.2007.07.006.

[36] Z. Chen, U. Gandhi, J. Lee, R. Wagoner, Variation and consistency of Young's modulus in steel, Journal of Materials Processing Technology 227 (2016) 227–243.

[37] M. Wang, R. Yang, A. Yu, DEM investigation of energy distribution and particle breakage in tumbling ball mills, Powder Technology 223 (2012) 83–91.

[38] D. R. Vyas, J. M. Ottino, R. M. Lueptow, P. B. Umbanhowar, Improved velocity-Verlet algorithm for the discrete element method, Computer Physics Communications 310 (2025) 109524.

[39] M. Ghadiri, Z. Zhang, Impact attrition of particulate solids. part 1: A theoretical model of chipping, Chemical Engineering Science 57 (17) (2002) 3659–3669.

[40] R. M. Christensen, Yield functions/failure criteria for isotropic materials, Proceedings of the Royal Society of London. Series A: Mathematical, Physical and Engineering Sciences 453 (1997) 1473–1491.

[41] W. Weibull, A statistical distribution function of wide applicability, Journal of Applied Mechanics (1951).

[42] Y. Hiramatsu, Y. Oka, Determination of the tensile strength of rock by a compression test of an irregular test piece, International Journal of Rock Mechanics and Mining Sciences & Geomechanics Abstracts 3 (2) (1966) 89–90. doi:https://doi.org/10.1016/0148-9062(66)90002-7.
URL https://www.sciencedirect.com/science/article/pii/0148906266900027

[43] G. McDowell, A. Amon, The application of Weibull statistics to the fracture of soil particles, Soils and Foundations 40 (5) (2000) 133–141.

[44] J. C. Jaeger, Failure of rocks under tensile conditions, International Journal of Rock Mechanics and Mining Sciences & Geomechanics Abstracts 4 (2) (1967) 219–227.

[45] Y. Nakata, Y. Kato, M. Hyodo, A. F. Hyde, H. Murata, One-dimensional compression behaviour of uniformly graded sand related to single particle crushing strength, Soils and Foundations 41 (2) (2001) 39–51.

[46] Y. Qing, Z. Qiu, Y. Tang, W. Deng, X. Zhang, J. Miu, S. Song, Effects of the particle shape and size on the single-particle breakage strength, Advances in Civil Engineering 2022 (1) (2022) 3386025.

[47] J. Wang, S. Chi, X. Zhou, X. Shao, Experimental and numerical investigation of the size effect of rockfill particles on crushing strength, Granular Matter 25 (3) (2023) 60. doi:10.1007/s10035-023-01346-7.

[48] T. Weinhart, S. Luding, A. R. Thornton, From discrete particles to continuum fields in mixtures, AIP Conference Proceedings 1542 (1) (2013) 1202–1205. arXiv:https://pubs.aip.org/aip/acp/article-pdf/1542/1/1202/11506634/1202_1_online.pdf, doi:10.1063/1.4812153.
URL https://doi.org/10.1063/1.4812153

[49] K. M. Hill, D. S. Tan, Segregation in dense sheared flows: gravity, temperature gradients, and stress partitioning, Journal of Fluid Mechanics 756 (2014) 54–88.

[50] A. P. Thompson, S. J. Plimpton, W. Mattson, General formulation of pressure and stress tensor for arbitrary many-body interaction potentials under periodic boundary conditions, Journal of Chemical Physics 131 (15) (2009) 154107.

[51] LAMMPS Developers, compute stress/atom, LAMMPS documentation, https://docs.lammps.org/compute_stress_atom.html, accessed 2025-08-21 (2025).

[52] Y. Zhang, G. Buscarnera, I. Einav, Grain size dependence of yielding in granular soils interpreted using fracture mechanics, breakage mechanics and Weibull statistics, Géotechnique 66 (2) (2016) 149–160.

[53] B. Mishra, Ball charge dynamics in a planetary mill, KONA Powder and Particle Journal 13 (0) (1995) 151–158.

[54] T. Iwasaki, H. Yamanouchi, Ball-impact energy analysis of wet tumbling mill using a modified discrete element method considering the velocity dependence of friction coefficient, Chemical Engineering Research and Design 163 (2020) 241–247.

[55] R. Cabiscol, T. Jansen, M. Marigo, C. Ness, Application of hydrodynamic lubrication in discrete element method (DEM) simulations of wet bead milling chambers, Powder Technology 384 (2021) 542–553.

[56] F. M. Katubilwa, Effect of ball size distribution on milling parameters, University of the Witwatersrand, Johannesburg (South Africa), 2008.

[57] H. Cho, J. Kwon, K. Kim, M. Mun, Optimum choice of the make-up ball sizes for maximum throughput in tumbling ball mills, Powder Technology 246 (2013) 625–634.

[58] S. L. Muketekelwa, Investigating the potential of using hydrocyclone-fine screen hybrid systems to improve the performance of classification circuits, Master's thesis, University of Cape Town (2017).

[59] H. Dündar, Investigating the benefits of replacing hydrocyclones with high-frequency fine screens in closed grinding circuit by simulation, Minerals Engineering 148 (2020) 106212.

[60] Y. Tsuji, T. Tanaka, T. Ishida, Lagrangian numerical simulation of plug flow of cohesionless particles in a horizontal pipe, Powder Technology 71 (3) (1992) 239–250.

Supplementary Information

Equation, figure, table and section numbers prefixed with S refer to this appendix; unprefixed numbers refer to the main report. References use the shared reference list preceding this appendix.

S1 Nomenclature

Symbols used in the main text and the Supplementary Information. Where a symbol appears in both the main text (M) and the Supplementary Information (S) it denotes the same quantity throughout.

Symbol	Where	Meaning
α	M, S	Impact angle, between the incoming grinding ball's velocity and $-\hat{\mathbf{n}}_1$; α_c is the critical impact angle bounding the trapped band.
γ	M, S	Obliquity angle, between the incoming grinding ball's velocity and the contact normal $\hat{\mathbf{n}}_2$; γ_c is the critical obliquity angle.
θ	M, S	Contact half-angle, $\theta = \frac{1}{2}(\alpha + \gamma)$, between the two contact normals. The impact, trapping and energy conditions all depend on the two collision angles only through θ.
R	M, S	Size ratio, $R = r_g/r_t$, of grinding-ball to target-particle radius.
μ	M, S	Sliding friction coefficient. Plain μ is the collision parameter; $\mu_{s,t}$ and $\mu_{s,g}$ are the same-material values and μ_{eff} the geometric mixture.
ϕ	M	Friction angle (friction-cone half-angle), $\phi = \arctan \mu$. The trapping condition is $\lvert\theta\rvert \le \phi$.
ρ	M, S	Mass density: ρ_t target particle (limestone), ρ_g grinding balls (steel).
ν	M	Poisson's ratio: ν_t target particle, ν_g grinding balls.
κ	M, S	Mindlin ratio of tangential to normal contact stiffness, $\kappa = k_t/k_n \approx 0.68$.
σ_{ij}	M	Average (virial) stress tensor in the target particle, with trace σ_{kk} and deviator s_{ij}.
σ_C, σ_T	M	Uniaxial compressive and tensile strengths of the target material, which calibrate the Christensen constants k_C and a_C.
σ_{pc}, $\sigma_{pc,0}$	M	Characteristic particle crushing stress and its value at the reference diameter d_0, from single-particle crushing tests (Weibull criterion).
δ	M, S	Normal contact overlap in the Hertz law; δ_1, δ_2 at contacts 1 and 2, δ_c the critical overlap at the fracture threshold, and δ_{max} the maximum overlap.
δ_t	S	Tangential relative displacement at a contact; $\delta_{t,1}$, $\delta_{t,2}$ at the two contacts. Locked to δ by the equilibrium condition $k_t\delta_t = -k_n\delta \tan\theta$.
δ_{ij}	M	Kronecker delta, in the deviatoric-stress definition of the Christensen criterion.
Δt	M	Integration timestep of the velocity-Verlet scheme, 1.0×10^{-7} s.
ψ_t, ψ_g	S	Angular displacement of the target particle and of the incoming grinding ball about the collision-plane normal.
η_0	S	Dashpot coefficient of the Tsuji normal damping term, calibrated internally by LAMMPS to the prescribed restitution coefficient.
ζ	M, S	Viscous damping ratio of the contact oscillator; ζ_{bin} for the isolated two-particle collision, ζ_{trap} for the trapped three-body compression mode.

Symbol	Where	Meaning
λ	M, S	Damping index, an equivalent form of ζ measuring how quickly the oscillation decays; λ_{bin} and λ_{trap}.
ω_0, ω_d	S	Undamped and damped angular frequencies of the auxiliary linear oscillator.
τ	M, S	Dimensionless phase of the damped contact oscillation, $\tau = \omega_d t$; τ_{pk} is the phase of the force peak and τ_F the force phase advance, $2 \arctan \lambda$.
Ψ	M, S	Force-delivery factor: peak contact force of the damped collision relative to the lossless one. Ψ_{bin} for the isolated binary contact, Ψ_{trap} for the trapped mode.
$\boldsymbol{\ell}_i$	M	Branch vector from the target-particle center to contact i, in the average-stress (Love–Weber) formula.
$\mathbf{T}_i$	S	Torque on the target particle about its center from the tangential spring at contact i.
$b(\theta)$	S	Overlap-to-mode-coordinate ratio of the trapped compression mode, $\delta = b\,X$.
π	M, S	The circle constant.
β	S	Dummy angle in quoted trigonometric identities; no physical meaning.

S2 Derivation of the energy–geometry factor

The derivation proceeds in four steps. The degrees of freedom and the contact-spring displacements are defined first in S2.1. Then the equations of motion of the target and grinding particles are analyzed. Neglecting the inertia of the target particle, quasi-static equilibrium of the target particle then forces the two contacts to share a single normal overlap δ, with the tangential displacement δ_t locked to it in S2.2. Eliminating the target particle's coordinates from the grinding particle's equations of motion reduces the collision to simple harmonic motion in a single coordinate, X, in S2.3, and partitioning the energy stored at peak compression yields the factor G in S2.4. Although this study uses nonlinear spring models, the derivation below uses the linear spring models for simplicity and to demonstrate the core idea. The generalization to the nonlinear spring models and the parameter evaluation are discussed at the end of S2.4.

S2.1 Contact kinematics

The target particle and the incoming grinding ball each have three degrees of freedom. The target particle has a center displacement $\mathbf{u} = (u_x, u_y)$ in the collision plane and an angular displacement ψ_t about the plane normal; the incoming grinding ball has a center displacement $\mathbf{U} = (U_x, U_y)$ in the collision plane and an angular displacement ψ_g about the plane normal; and the fixed grinding ball has no degrees of freedom. Both rotation angles are taken positive counterclockwise about the unit normal $\hat{\mathbf{z}}$, directed out of the collision plane. Adopt Cartesian axes in the collision plane with the x-axis along $\hat{\mathbf{n}}_1$, so that $\hat{\mathbf{n}}_1 = (1, 0)$ and $\hat{\mathbf{t}}_1 = (0, 1)$. In this frame $\hat{\mathbf{n}}_2$ has the direction $(-\cos 2\theta,\ -\sin 2\theta)$, where $\theta = \frac{1}{2}(\alpha + \gamma)$ is the half-angle defined in the main text, and $\hat{\mathbf{t}}_2 = \hat{\mathbf{z}} \times \hat{\mathbf{n}}_2 = (\sin 2\theta,\ -\cos 2\theta)$. The impact velocity of the incoming grinding ball is

$$\mathbf{v} = -\,v\,(\cos\alpha,\ \sin\alpha). \tag{S1}$$

Define $\hat{\mathbf{n}}_a$ as the unit vector along the bisector of $\hat{\mathbf{n}}_1$ and $-\hat{\mathbf{n}}_2$, where $\hat{\mathbf{n}}_a = (\cos\theta, \sin\theta)$, and define the unit vector perpendicular to $\hat{\mathbf{n}}_a$ as $\hat{\mathbf{q}} = (-\sin\theta, \cos\theta)$.

Each contact can be modeled with two linear springs: a normal spring of stiffness k_n and a tangential spring of stiffness k_t. The normal spring is compressed by the relative displacement of the two spheres along the contact normal, and the tangential spring is stretched by their relative displacement along the contact tangent; because the contact does not slip, this tangential relative displacement is the relative displacement of the two surface points that meet at the contact. Since the fixed grinding ball is immobile, the normal overlap δ_1 at contact 1 is produced by the center displacement of the target particle alone. With δ_1 defined positive in the $-\hat{\mathbf{n}}_1$ direction,

$$\delta_1 = -\mathbf{u} \cdot \hat{\mathbf{n}}_1 = -u_x. \tag{S2}$$

The tangential displacement $\delta_{t,1}$ is defined as the displacement of the surface point of the target particle along the $+\hat{\mathbf{t}}_1$ direction, which yields

$$\delta_{t,1} = u_y - r_t\psi_t. \tag{S3}$$

For the contact between the target particle and the incoming grinding ball, the normal overlap δ_2 is defined as the relative center displacement of the incoming grinding ball with respect to the target particle, projected onto $\hat{\mathbf{n}}_2$:

$$\delta_2 = (\mathbf{U} - \mathbf{u}) \cdot \hat{\mathbf{n}}_2. \tag{S4}$$

The tangential displacement $\delta_{t,2}$ is defined as the displacement of the surface point of the incoming grinding ball relative to that of the target particle, projected onto $+\hat{\mathbf{t}}_2$, which yields

$$\delta_{t,2} = (\mathbf{U} - \mathbf{u}) \cdot \hat{\mathbf{t}}_2 + r_t\psi_t + r_g\psi_g. \tag{S5}$$

S2.2 Quasi-static equilibrium

Since the mass of the target particle is much smaller than that of the grinding particle, the equations of motion of the target particle can be simplified to quasi-static force and torque equilibrium equations by neglecting its inertia.

For the forces, each normal spring exerts a compressive restoring force on the target particle along the contact normal:

$$\mathbf{F}_{1,n} = +k_n\delta_1\,\hat{\mathbf{n}}_1, \quad \mathbf{F}_{2,n} = +k_n\delta_2\,\hat{\mathbf{n}}_2. \tag{S6}$$

Each tangential spring exerts a restoring force on the target particle that opposes the relative tangential displacement:

$$\mathbf{F}_{1,t} = -k_t\delta_{t,1}\,\hat{\mathbf{t}}_1, \quad \mathbf{F}_{2,t} = +k_t\delta_{t,2}\,\hat{\mathbf{t}}_2. \tag{S7}$$

The tangential forces act at the contact points, located at $-r_t\hat{\mathbf{n}}_1$ and $-r_t\hat{\mathbf{n}}_2$ from the center of the target particle, and therefore exert torques on it:

$$\mathbf{T}_1 = (-r_t\hat{\mathbf{n}}_1) \times (-k_t\delta_{t,1}\,\hat{\mathbf{t}}_1) = +\,k_t r_t\delta_{t,1}\,\hat{\mathbf{z}}, \quad \mathbf{T}_2 = (-r_t\hat{\mathbf{n}}_2) \times (+k_t\delta_{t,2}\,\hat{\mathbf{t}}_2) = -\,k_t r_t\delta_{t,2}\,\hat{\mathbf{z}}. \tag{S8}$$

The torque balance of the target particle yields

$$k_t r_t \delta_{t,1} - k_t r_t \delta_{t,2} = 0, \tag{S9}$$

which simplifies to

$$\delta_{t,1} = \delta_{t,2} = \delta_t. \tag{S10}$$

The force balance yields

$$k_n \delta_1 \, \hat{\mathbf{n}}_1 + k_n \delta_2 \, \hat{\mathbf{n}}_2 - k_t \, \delta_t \, \hat{\mathbf{t}}_1 + k_t \, \delta_t \, \hat{\mathbf{t}}_2 = \mathbf{0}. \tag{S11}$$

Projecting Equation (S11) onto $\hat{\mathbf{n}}_1$ and $\hat{\mathbf{t}}_1$ requires the dot products

$$\hat{\mathbf{n}}_2 \cdot \hat{\mathbf{n}}_1 = -\cos 2\theta, \quad \hat{\mathbf{t}}_2 \cdot \hat{\mathbf{n}}_1 = \sin 2\theta, \quad \hat{\mathbf{n}}_2 \cdot \hat{\mathbf{t}}_1 = -\sin 2\theta, \quad \hat{\mathbf{t}}_2 \cdot \hat{\mathbf{t}}_1 = -\cos 2\theta. \tag{S12}$$

Projecting Equation (S11) onto $\hat{\mathbf{n}}_1$ yields

$$k_n \delta_1 - k_n \delta_2 \cos 2\theta + k_t \, \delta_t \, \sin 2\theta = 0. \tag{S13}$$

Projecting Equation (S11) onto $\hat{\mathbf{t}}_1$ yields

$$-k_t \, \delta_t - k_n \delta_2 \sin 2\theta - k_t \, \delta_t \, \cos 2\theta = 0. \tag{S14}$$

Rearranging Equation (S14) gives

$$-k_t \, \delta_t \, (1 + \cos 2\theta) = k_n \delta_2 \sin 2\theta. \tag{S15}$$

Note that $\frac{\sin 2\theta}{1+\cos 2\theta} = \tan\theta$, which simplifies Equation (S15) to

$$k_t \, \delta_t = -k_n \delta_2 \tan\theta. \tag{S16}$$

Equation (S16) states that each sticking contact carries a tangential-to-normal force ratio of magnitude $\tan\theta$, which is consistent with the trapping condition $\mu \geq \tan\theta$ in the main text. Substituting Equation (S16) into Equation (S13) expresses everything in terms of the normal spring force and gives

$$k_n \delta_1 - k_n \delta_2 \cos 2\theta - k_n \delta_2 \tan\theta \, \sin 2\theta = 0, \tag{S17}$$

which simplifies to

$$k_n \delta_1 - k_n \delta_2 (\cos 2\theta + \tan\theta \, \sin 2\theta) = 0. \tag{S18}$$

Note that $\cos 2\theta + \tan\theta \sin 2\theta = \cos 2\theta + 2\sin^2\theta = 1$, which simplifies Equation (S18) to

$$\delta_1 = \delta_2 = \delta. \tag{S19}$$

Thus, the target particle experiences the same normal overlap δ at both contacts.

Substituting Equation (S19) into Equation (S16) yields

$$\delta_t = -\frac{\delta \tan\theta}{\kappa}, \tag{S20}$$

where κ is defined as the ratio of the tangential to the normal stiffness:

$$\kappa = \frac{k_t}{k_n}. \tag{S21}$$

S2.3 Reduction to a single oscillator

Now we consider the kinematics and the equations of motion of the grinding particle.

For the normal displacement, substituting Equation (S4) into Equation (S19) gives

$$\mathbf{U}\cdot\hat{\mathbf{n}}_2 - \mathbf{u}\cdot\hat{\mathbf{n}}_2 = \delta. \tag{S22}$$

Expanding the dot product $\mathbf{u}\cdot\hat{\mathbf{n}}_2$ gives

$$\mathbf{U}\cdot\hat{\mathbf{n}}_2 + u_x\cos 2\theta + u_y \sin 2\theta = \delta. \tag{S23}$$

Substituting $u_x = -\delta$ from Equation (S2) and Equation (S19), and rearranging, gives

$$u_y \sin 2\theta = \delta\,(1+\cos 2\theta) - \mathbf{U}\cdot\hat{\mathbf{n}}_2. \tag{S24}$$

Applying the double-angle identity $\cos 2\theta = 2\cos^2\theta - 1$ gives

$$u_y \sin 2\theta = 2\delta\cos^2\theta - \mathbf{U}\cdot\hat{\mathbf{n}}_2. \tag{S25}$$

For the tangential displacement, adding Equation (S3) and Equation (S5) eliminates $r_t\psi_t$:

$$2\delta_t = u_y + (\mathbf{U}-\mathbf{u})\cdot\hat{\mathbf{t}}_2 + r_g\psi_g. \tag{S26}$$

Expanding the dot product $\mathbf{u}\cdot\hat{\mathbf{t}}_2$ gives

$$2\delta_t = u_y + \mathbf{U}\cdot\hat{\mathbf{t}}_2 - u_x\sin 2\theta + u_y\cos 2\theta + r_g\psi_g. \tag{S27}$$

Substituting $u_x = -\delta$ gives

$$2\delta_t = u_y\,(1+\cos 2\theta) + \mathbf{U}\cdot\hat{\mathbf{t}}_2 + \delta\sin 2\theta + r_g\psi_g. \tag{S28}$$

Applying the double-angle identities $\cos 2\theta = 2\cos^2\theta - 1$ and $\sin 2\theta = 2\sin\theta\cos\theta$, and rearranging, gives

$$2u_y\cos^2\theta = 2\delta_t - 2\delta\sin\theta\cos\theta - \mathbf{U}\cdot\hat{\mathbf{t}}_2 - r_g\psi_g. \tag{S29}$$

Multiplying both sides of Equation (S25) by $\cot\theta$ gives

$$2u_y \cos^2\theta = 2\delta \cos^2\theta \cot\theta - (\mathbf{U}\cdot\hat{\mathbf{n}}_2)\cot\theta. \tag{S30}$$

The left-hand sides of Equation (S29) and Equation (S30) are identical, so equating their right-hand sides gives

$$2\delta \cos^2\theta \cot\theta - (\mathbf{U}\cdot\hat{\mathbf{n}}_2)\cot\theta = 2\delta_t - 2\delta \sin\theta\cos\theta - \mathbf{U}\cdot\hat{\mathbf{t}}_2 - r_g\psi_g. \tag{S31}$$

Substituting Equation (S20) into Equation (S31) gives

$$2\delta \cos^2\theta \cot\theta - (\mathbf{U}\cdot\hat{\mathbf{n}}_2)\cot\theta = -\frac{2\delta\tan\theta}{\kappa} - 2\delta \sin\theta\cos\theta - \mathbf{U}\cdot\hat{\mathbf{t}}_2 - r_g\psi_g, \tag{S32}$$

which simplifies to

$$2\delta\Big[\frac{\cos^3\theta}{\sin\theta} + \sin\theta\cos\theta + \frac{\tan\theta}{\kappa}\Big] = (\mathbf{U}\cdot\hat{\mathbf{n}}_2)\cot\theta - \mathbf{U}\cdot\hat{\mathbf{t}}_2 - r_g\psi_g. \tag{S33}$$

Note that

$$\frac{\cos^3\theta}{\sin\theta} + \sin\theta\cos\theta = \cot\theta, \tag{S34}$$

which simplifies the left-hand side of Equation (S33) to

$$2\delta\Big(\cot\theta + \frac{\tan\theta}{\kappa}\Big) = \frac{2\delta\,(\kappa\cos^2\theta + \sin^2\theta)}{\kappa\sin\theta\cos\theta}. \tag{S35}$$

The first two terms on the right-hand side of Equation (S33) combine over the common denominator $\sin\theta$:

$$(\mathbf{U}\cdot\hat{\mathbf{n}}_2)\cot\theta - \mathbf{U}\cdot\hat{\mathbf{t}}_2 = \frac{\mathbf{U}\cdot\big(\hat{\mathbf{n}}_2\cos\theta - \hat{\mathbf{t}}_2\sin\theta\big)}{\sin\theta}. \tag{S36}$$

Note that

$$\hat{\mathbf{n}}_2\cos\theta - \hat{\mathbf{t}}_2\sin\theta = \begin{pmatrix} -\cos 2\theta\cos\theta - \sin 2\theta\sin\theta \\ -\sin 2\theta\cos\theta + \cos 2\theta\sin\theta \end{pmatrix} = \begin{pmatrix} -\cos\theta \\ -\sin\theta \end{pmatrix} = -\hat{\mathbf{n}}_a, \tag{S37}$$

which simplifies the right-hand side of Equation (S36) to

$$(\mathbf{U}\cdot\hat{\mathbf{n}}_2)\cot\theta - \mathbf{U}\cdot\hat{\mathbf{t}}_2 = -\frac{\mathbf{U}\cdot\hat{\mathbf{n}}_a}{\sin\theta}. \tag{S38}$$

Therefore, Equation (S33) simplifies to

$$\delta\,\frac{2\,(\kappa\cos^2\theta + \sin^2\theta)}{\kappa\sin\theta\cos\theta} = -\frac{\mathbf{U}\cdot\hat{\mathbf{n}}_a}{\sin\theta} - r_g\psi_g. \tag{S39}$$

Rearranging to isolate δ yields

$$\delta = -\frac{\kappa\cos\theta\,\big(\mathbf{U}\cdot\hat{\mathbf{n}}_a + r_g\psi_g\sin\theta\big)}{2\,\big(\kappa\cos^2\theta + \sin^2\theta\big)}. \tag{S40}$$

Let the projection of **U** onto $\hat{\mathbf{n}}_a$ be $U_a = \mathbf{U} \cdot \hat{\mathbf{n}}_a$, the projection of **U** onto $\hat{\mathbf{q}}$ be $U_q = \mathbf{U} \cdot \hat{\mathbf{q}}$, and define the scaled rotation $s_g = r_g \psi_g$, which has dimensions of length.

Therefore, Equation (S40) can be expressed as

$$\delta = -\frac{\kappa \cos\theta \left(U_a + s_g \sin\theta\right)}{2\left(\kappa \cos^2\theta + \sin^2\theta\right)}. \tag{S41}$$

Define

$$X = -\left(U_a + s_g \sin\theta\right) \tag{S42}$$

and

$$b = \frac{\kappa \cos\theta}{2\left(\kappa \cos^2\theta + \sin^2\theta\right)}, \tag{S43}$$

so that Equation (S41) can be expressed as

$$\delta = b\, X. \tag{S44}$$

For the dynamics of the grinding particle, the incoming grinding ball has mass $M = \rho_g V_g$, where ρ_g is the grinding-ball density and $V_g = \frac{4}{3}\pi r_g^3$ the ball volume, and a moment of inertia $I = \frac{2}{5} M r_g^2$ about its center, for a solid sphere.

The rotational kinetic energy is expressed in terms of $\dot{s_g} = r_g \dot{\psi_g}$:

$$\tfrac{1}{2} I \dot{\psi_g}^2 = \tfrac{1}{5} M r_g^2 \dot{\psi_g}^2 = \tfrac{1}{5} M \dot{s_g}^2. \tag{S45}$$

Combining translation and rotation gives the total kinetic energy E_{kin} of the incoming grinding ball in the coordinates (U_a, U_q, s_g):

$$E_{\text{kin}} = \tfrac{1}{2} M \left(\dot{U}_a^2 + \dot{U}_q^2\right) + \tfrac{1}{2} I \dot{\psi_g}^2 = \tfrac{1}{2} M \dot{U}_a^2 + \tfrac{1}{2} M \dot{U}_q^2 + \tfrac{1}{5} M \dot{s_g}^2. \tag{S46}$$

The elastic potential energy E_{el} stored in the two contacts is the sum of the two normal springs at the common overlap δ and the two tangential springs at the common tangential displacement δ_t:

$$E_{\text{el}} = 2 \cdot \tfrac{1}{2} k_n \delta^2 + 2 \cdot \tfrac{1}{2} k_t\, \delta_t^2 = k_n \delta^2 + k_t\, \delta_t^2. \tag{S47}$$

Substituting Equation (S20) and Equation (S21) into Equation (S47) and simplifying yields

$$E_{\text{el}} = k_n \delta^2 \left(1 + \frac{\tan^2\theta}{\kappa}\right) = k_n \delta^2\, \frac{\kappa \cos^2\theta + \sin^2\theta}{\kappa \cos^2\theta}. \tag{S48}$$

The effective stiffness K^* is defined as the second derivative of the potential energy with respect to X, evaluated by substituting Equation (S44) into Equation (S48):

$$K^* = \frac{d^2 E_{\text{el}}}{dX^2} = 2 k_n b^2\, \frac{\kappa \cos^2\theta + \sin^2\theta}{\kappa \cos^2\theta}. \tag{S49}$$

Substituting the expression for b from Equation (S43) and simplifying yields the expression for K^*:

$$K^* = \frac{\kappa\, k_n}{2\,(\kappa \cos^2\theta + \sin^2\theta)}. \tag{S50}$$

Thus, the total elastic potential energy is

$$E_{\text{el}}(X) = \tfrac{1}{2}\, K^* X^2. \tag{S51}$$

As stated in the assumption that the inertia of the target particle is negligible, its coordinates adjust instantaneously to the motion of the incoming grinding ball, and $E_{\text{el}}(X)$ acts as the potential energy governing the remaining degrees of freedom (U_a, U_q, s_g). The equations of motion of the grinding particle give

$$M\ddot{U}_a = -\frac{\partial E_{\text{el}}}{\partial U_a}, \qquad \tfrac{2}{5} M \ddot{s_g} = -\frac{\partial E_{\text{el}}}{\partial s_g}, \qquad M\ddot{U}_q = -\frac{\partial E_{\text{el}}}{\partial U_q}. \tag{S52}$$

Because E_{el} depends on (U_a, s_g) only through X in Equation (S42), the required derivatives of X are

$$\frac{\partial X}{\partial U_a} = -1, \qquad \frac{\partial X}{\partial s_g} = -\sin\theta, \qquad \frac{\partial X}{\partial U_q} = 0. \tag{S53}$$

Applying the chain rule to $E_{\text{el}}(X)$ with Equation (S53) gives

$$\frac{\partial E_{\text{el}}}{\partial U_a} = -E'_{\text{el}}(X), \qquad \frac{\partial E_{\text{el}}}{\partial s_g} = -E'_{\text{el}}(X)\sin\theta, \qquad \frac{\partial E_{\text{el}}}{\partial U_q} = 0. \tag{S54}$$

Substituting Equation (S54) into Equation (S52) yields the equations of motion:

$$M\ddot{U}_a = E'_{\text{el}}(X), \qquad \tfrac{2}{5} M \ddot{s_g} = E'_{\text{el}}(X)\sin\theta, \qquad M\ddot{U}_q = 0. \tag{S55}$$

Differentiating Equation (S42) twice and substituting the first two equations of Equation (S55) gives

$$\ddot{X} = -\big(\ddot{U}_a + \ddot{s_g}\sin\theta\big) = -E'_{\text{el}}(X)\Big(\frac{1}{M} + \frac{5\sin^2\theta}{2M}\Big) = -\,K^* X\,\frac{2 + 5\sin^2\theta}{2M}. \tag{S56}$$

Define the effective mass M^* as

$$M^* = \frac{2M}{2 + 5\sin^2\theta}, \tag{S57}$$

so that the equation takes the standard form of simple harmonic motion:

$$M^*\ddot{X} = -\,K^* X. \tag{S58}$$

The corresponding velocity relation follows by differentiating Equation (S42) once:

$$\dot{X} = -\big(\dot{U}_a + \dot{s_g}\sin\theta\big). \tag{S59}$$

The initial conditions are $\dot{U}_a(0) = \mathbf{v}\cdot\hat{\mathbf{n}}_a$ and $\dot{s_g}(0) = 0$, which give

$$\dot{X}(0) = -\,\mathbf{v}\cdot\hat{\mathbf{n}}_a = v\,(\cos\alpha\cos\theta + \sin\alpha\sin\theta) = v\cos(\theta - \alpha). \tag{S60}$$

S2.4 Energy partition

The energy of the simple harmonic oscillator,

$$E_{\text{mode}} = \tfrac{1}{2}M^*\dot{X}^2 + \tfrac{1}{2}K^*X^2, \tag{S61}$$

is conserved. At $t = 0$ the springs are unloaded, so $X(0) = 0$ and

$$E_{\text{mode}} = \tfrac{1}{2}M^*\dot{X}(0)^2 = \tfrac{1}{2}M^*(v\cos(\theta-\alpha))^2. \tag{S62}$$

At peak compression $\dot{X} = 0$, so the entire mode energy is momentarily stored as elastic potential energy, $E_{\text{el}} = E_{\text{mode}}$.

The energy–geometry factor G is the product of two fractions: the fraction of the initial kinetic energy that is converted to elastic potential at peak compression, and the fraction of that elastic energy, $E_{\text{el},n}$, that is stored in the normal springs and contributes to compression. The first fraction is evaluated as

$$\frac{E_{\text{mode}}}{\frac{1}{2}Mv^2} = \frac{\frac{1}{2}\left(\frac{2M}{2+5\sin^2\theta}\right)(v\cos(\theta-\alpha))^2}{\frac{1}{2}Mv^2} = \cos^2(\theta-\alpha)\,\frac{2}{2+5\sin^2\theta}. \tag{S63}$$

The second fraction is evaluated as

$$\frac{E_{\text{el},n}}{E_{\text{el}}} = \frac{k_n\delta^2}{k_n\delta^2\,(\kappa\cos^2\theta+\sin^2\theta)/(\kappa\cos^2\theta)} = \frac{\kappa\cos^2\theta}{\kappa\cos^2\theta+\sin^2\theta}. \tag{S64}$$

The product of Equation (S63) and Equation (S64) gives the energy–geometry factor

$$G = \cos^2(\theta-\alpha)\,\frac{2\kappa\,\cos^2\theta}{\left(\kappa\cos^2\theta+\sin^2\theta\right)\left(2+5\sin^2\theta\right)}. \tag{S65}$$

Substituting $\theta = \frac{1}{2}(\alpha+\gamma)$ and simplifying yields

$$G(\alpha,\gamma) = \frac{2\kappa\left(\cos\alpha+\cos\gamma\right)^2}{\left((\kappa+1)+(\kappa-1)\cos(\alpha+\gamma)\right)\left(9-5\cos(\alpha+\gamma)\right)}. \tag{S66}$$

The above analysis is based on linear spring models for the normal and tangential contacts, i.e., k_n and k_t are constant. Since the manuscript uses Hertz and Mindlin models for the normal and tangential contact forces with k_n and k_t as functions of δ, we follow the same procedure using nonconstant k_n and k_t. Although some of the prefactors in the energy Equations (S47)–(S51), (S56) and (S61) are changed, the expression for the energy-geometry factor G, Equation (S66), remains the same.

The reason is that both contact forces are proportional to the contact radius $a = \sqrt{R^*\delta}$, so that $F^n = k_n a\delta$ and $F^t = k_t a\delta_t$. The factor a cancels from the force balance, leaving $\delta_t = -\delta\tan\theta/\kappa$ with $\kappa = k_t/k_n$ exactly as in Equation (S20). Along the loading path, the ratio of stored elastic energies is therefore

$$\frac{E_{\text{el},t}}{E_{\text{el},n}} = \frac{\int F^t\,d\delta_t}{\int F^n\,d\delta} = \frac{\tan^2\theta}{\kappa}, \tag{S67}$$

which is the ratio already used in Equation (S48). The kinematic factor of Equation (S63) involves only

inertia and the constraint $\delta = bX$, neither of which depends on the force law.

For the tangential-to-normal stiffness parameter κ, both stiffnesses of a Hertz–Mindlin contact are proportional to the contact radius a, so their ratio is a constant of the material pair. The normal stiffness follows from the effective modulus of the pair, $k_n = \frac{4}{3}E^*a$, and the Mindlin tangential stiffness in this formulation is built from that same effective modulus, $k_t = 8Ga$ with $G = E^*/[4(2-\nu)(1+\nu)]$, so that

$$\kappa = \frac{3}{2\,(2-\nu)(1+\nu)} \approx 0.68, \tag{S68}$$

where $\nu = \sqrt{\nu_t \nu_g}$ is the mixed Poisson's ratio of Table 1. Measured directly from the simulated contact forces and displacements while the contacts stick, $\kappa = 0.678$.

S3 Derivation of the damping factor Ψ_{trap}

S3.1 Setup and inputs

The critical velocity $v_{c,0}$ in the main text is obtained from a lossless energy balance, whereas the DEM contact model includes viscous damping through the restitution coefficient e. The purpose of this derivation is to quantify how that damping changes the peak force transmitted through a particle trapped between two grinding balls. We define the resulting force-delivery factor as Ψ_{trap} and show that $v_{c,\text{damp}} = v_{c,0}\Psi_{\text{trap}}^{-5/6}$. For the production values $e = 0.5$ and $R = 4$, the correction is only 1.7%.

We consider the head-on configuration in which a target particle (limestone in the production simulations) has radius r_t and mass m_t and is trapped between a fixed grinding ball and an incoming grinding ball. Both grinding balls have radius r_g, the incoming ball has mass m_g, and all three centers remain collinear. The size ratio is $R \equiv r_g/r_t$. Throughout this derivation, italic e denotes the restitution coefficient and upright e denotes Euler's number. The symbol k_H denotes the lumped Hertz stiffness; the Weibull modulus m of the main text does not appear in this derivation, and all masses carry subscripts.

We begin with the Hertz normal force law

$$F(\delta) \;=\; k_H\,\delta^{3/2}, \qquad k_H \;\equiv\; \tfrac{4}{3}\,E^*\sqrt{R^*}. \tag{S69}$$

Integrating Equation (S69) from zero overlap to δ gives the elastic energy stored in one contact,

$$E_{\text{el}}(\delta) \;=\; \int_0^{\delta} k_H\,\delta'^{3/2}\,d\delta' \;=\; \tfrac{2}{5}\,k_H\,\delta^{5/2}. \tag{S70}$$

For a binary collision between bodies of masses m_1 and m_2, the overlap coordinate has the reduced mass

$$m^* \;=\; \frac{m_1 m_2}{m_1 + m_2}. \tag{S71}$$

Accordingly, the kinetic energy associated with the overlap is $\frac{1}{2}m^*\dot{\delta}^2$, and its equation of motion is written using $m^*\ddot{\delta}$.

In a lossless collision, the incident kinetic energy is stored entirely as elastic contact energy at maximum

compression. If $\dot{\delta}_0$ is the initial approach speed and $\delta_{\max}$ is the maximum overlap, then

$$\tfrac{1}{2}\, m^* \dot{\delta}_0^2 \;=\; E_{\mathrm{el}}(\delta_{\max}) \;=\; \tfrac{2}{5}\, k_H\, \delta_{\max}^{5/2}. \tag{S72}$$

Solving for the maximum overlap gives

$$\delta_{\max} \;=\; \left(\frac{\tfrac{5}{4}\, m^* \dot{\delta}_0^2}{k} \right)^{2/5}. \tag{S73}$$

Because the Hertz force increases monotonically with overlap, substituting Equation (S73) into Equation (S69) gives the lossless peak force:

$$F_{\max}^{\mathrm{undamped}} \;=\; k_H\, \delta_{\max}^{3/2} \;=\; k_H \left(\frac{\tfrac{5}{4}\, m^* \dot{\delta}_0^2}{k} \right)^{3/5} \;=\; k_H^{2/5} \left(\tfrac{5}{4}\, m^* \right)^{3/5} \dot{\delta}_0^{6/5}. \tag{S74}$$

At the same incident speed, damping changes the peak total contact force. Define the force-delivery factor as

$$\Psi \;\equiv\; \frac{F_{\max}^{\mathrm{damped}}}{F_{\max}^{\mathrm{undamped}}}. \tag{S75}$$

Let F_c be the force required for fracture. This threshold depends on the particle strength and geometry, not on the damping model, so it is the same in the undamped and damped descriptions. Equation (S133) will show that the damped peak retains the same $\dot{\delta}_0^{6/5}$ scaling as the undamped peak. Define the speed-independent force coefficient

$$C_F \;\equiv\; k_H^{2/5} \left(\tfrac{5}{4}\, m^* \right)^{3/5}, \qquad F_{\max}^{\mathrm{undamped}} \;=\; C_F\, \dot{\delta}_0^{6/5}. \tag{S76}$$

The corresponding damped peak is

$$F_{\max}^{\mathrm{damped}} \;=\; \Psi\, C_F\, \dot{\delta}_0^{6/5}. \tag{S77}$$

At the two critical velocities, each peak force equals F_c:

$$C_F\, v_{c,0}^{6/5} \;=\; F_c, \qquad \Psi\, C_F\, v_{c,\mathrm{damp}}^{6/5} \;=\; F_c. \tag{S78}$$

Dividing the two relations gives

$$\Psi \left(\frac{v_{c,\mathrm{damp}}}{v_{c,0}} \right)^{6/5} \;=\; 1. \tag{S79}$$

Therefore,

$$\frac{v_{c,\mathrm{damp}}}{v_{c,0}} \;=\; \Psi^{-5/6}. \tag{S80}$$

Thus, once Ψ is known, the damping correction to the critical velocity follows immediately.

S3.2 The damped contact law

LAMMPS represents the normal contact as a Hertz spring in parallel with a Tsuji dashpot [60]. The spring contributes $k_H \delta^{3/2}$, while the dashpot contributes $\eta_0 \delta^{1/4} \dot{\delta}$. The constant η_0 is calibrated internally so

that an isolated head-on binary collision has the prescribed restitution coefficient e; the $\delta^{1/4}$ dependence makes this restitution independent of impact speed. The overlap equation is therefore

$$m^* \ddot{\delta} \;=\; -\,k_H\,\delta^{3/2} \;-\; \eta_0\,\delta^{1/4}\,\dot{\delta}. \tag{S81}$$

The calibration $e \mapsto \eta_0$ is tied to this binary collision and its reduced mass. That distinction becomes important when the same dashpot is applied to the trapped three-body mode.

S3.3 A damped linear oscillator

We first solve an auxiliary underdamped linear oscillator. Section S3.4 will show that its phase-space trajectory is identical to that of the nonlinear Hertz contact after a change of coordinate.

Consider a linear oscillator of mass $\tilde{m}$, stiffness k_H, and dashpot coefficient η_0, with $y(0) = 0$ and $\dot{y}(0) = \dot{\delta}_0$:

$$\tilde{m}\,\ddot{y} \;+\; \eta_0\,\dot{y} \;+\; k_H\,y \;=\; 0. \tag{S82}$$

Define the undamped natural frequency, damping ratio, and damped frequency by

$$\omega_0 \;\equiv\; \sqrt{k/\tilde{m}}, \qquad \zeta \;\equiv\; \frac{\eta_0}{2\tilde{m}\,\omega_0}, \qquad \omega_d \;\equiv\; \omega_0\sqrt{1-\zeta^2}. \tag{S83}$$

The relevant regime is underdamped, $0 \le \zeta < 1$. Using the exponential trial solution $y = \mathrm{e}^{wt}$ gives

$$y \;=\; \mathrm{e}^{wt}, \qquad \dot{y} \;=\; w\,\mathrm{e}^{wt}, \qquad \ddot{y} \;=\; w^2\,\mathrm{e}^{wt}. \tag{S84}$$

Substitution into Equation (S82) yields the characteristic equation

$$\tilde{m}\,w^2 \;+\; \eta_0\,w \;+\; k_H \;=\; 0. \tag{S85}$$

Its roots are

$$w \;=\; \frac{-\eta_0 \pm \sqrt{\eta_0^2 - 4\tilde{m}k_H}}{2\tilde{m}}. \tag{S86}$$

Using $\eta_0 = 2\tilde{m}\zeta\omega_0$ and $k_H = \tilde{m}\omega_0^2$, the discriminant becomes

$$\eta_0^2 - 4\tilde{m}k_H \;=\; (2\tilde{m}\,\zeta\omega_0)^2 - 4\tilde{m}^2\omega_0^2 \;=\; (2\tilde{m}\,\omega_0)^2\left(\zeta^2 - 1\right). \tag{S87}$$

Because $\zeta < 1$, these roots form a complex-conjugate pair:

$$w \;=\; -\zeta\omega_0 \;\pm\; i\,\omega_0\sqrt{1-\zeta^2} \;=\; -\zeta\omega_0 \;\pm\; i\,\omega_d. \tag{S88}$$

Euler's identity gives, for any angle β,

$$\mathrm{e}^{\pm i\beta} \;=\; \cos\beta \;\pm\; i\sin\beta. \tag{S89}$$

Hence the two exponential solutions can be written as

$$\mathrm{e}^{(-\zeta\omega_0 \pm i\omega_d)t} \;=\; \mathrm{e}^{-\zeta\omega_0 t}\,\mathrm{e}^{\pm i\omega_d t} \;=\; \mathrm{e}^{-\zeta\omega_0 t}\big[\cos(\omega_d t) \pm i\sin(\omega_d t)\big]. \tag{S90}$$

Taking their sum and difference produces the corresponding real basis functions:

$$\begin{aligned}
\tfrac{1}{2}\Big[\mathrm{e}^{(-\zeta\omega_0+i\omega_d)t}+\mathrm{e}^{(-\zeta\omega_0-i\omega_d)t}\Big] &= \tfrac{1}{2}\,\mathrm{e}^{-\zeta\omega_0 t}\big[\cos(\omega_d t)+i\sin(\omega_d t)+\cos(\omega_d t)-i\sin(\omega_d t)\big] \\
&= \mathrm{e}^{-\zeta\omega_0 t}\cos(\omega_d t), \\
\tfrac{1}{2i}\Big[\mathrm{e}^{(-\zeta\omega_0+i\omega_d)t}-\mathrm{e}^{(-\zeta\omega_0-i\omega_d)t}\Big] &= \tfrac{1}{2i}\,\mathrm{e}^{-\zeta\omega_0 t}\big[\cos(\omega_d t)+i\sin(\omega_d t)-\cos(\omega_d t)+i\sin(\omega_d t)\big] \\
&= \tfrac{1}{2i}\,\mathrm{e}^{-\zeta\omega_0 t}\,\big[\,2i\sin(\omega_d t)\big] \;=\; \mathrm{e}^{-\zeta\omega_0 t}\sin(\omega_d t).
\end{aligned} \tag{S91}$$

The general real solution is therefore

$$y(t) \;=\; \mathrm{e}^{-\zeta\omega_0 t}\big[A\cos(\omega_d t)+B\sin(\omega_d t)\big]. \tag{S92}$$

The condition $y(0)=0$ gives

$$y(0) \;=\; A \;=\; 0. \tag{S93}$$

Differentiating the remaining term gives

$$\dot{y}(t) \;=\; B\,\mathrm{e}^{-\zeta\omega_0 t}\big[\omega_d\cos(\omega_d t)-\zeta\omega_0\sin(\omega_d t)\big]. \tag{S94}$$

The condition $\dot{y}(0)=\dot{\delta}_0$ then gives

$$\dot{y}(0) \;=\; B\,\omega_d \;=\; \dot{\delta}_0, \qquad B \;=\; \frac{\dot{\delta}_0}{\omega_d}. \tag{S95}$$

Thus,

$$y(t) \;=\; \frac{\dot{\delta}_0}{\omega_d}\,\mathrm{e}^{-\zeta\omega_0 t}\sin(\omega_d t), \qquad \dot{y}(t) \;=\; \dot{\delta}_0\,\mathrm{e}^{-\zeta\omega_0 t}\Big[\cos(\omega_d t)-\frac{\zeta\omega_0}{\omega_d}\sin(\omega_d t)\Big]. \tag{S96}$$

It is convenient to introduce the dimensionless damping index

$$\lambda \;\equiv\; \frac{\zeta\omega_0}{\omega_d}. \tag{S97}$$

The first return to $y=0$ occurs at the separation time

$$t_{\mathrm{sep}} \;=\; \frac{\pi}{\omega_d}. \tag{S98}$$

At this instant,

$$\dot{y}(t_{\mathrm{sep}}) \;=\; -\,\dot{\delta}_0\,\mathrm{e}^{-\pi\zeta\omega_0/\omega_d}. \tag{S99}$$

The restitution coefficient is the ratio of the separation and approach speeds, so

$$e \;=\; \frac{|\dot{y}(t_{\mathrm{sep}})|}{\dot{\delta}_0} \;=\; \mathrm{e}^{-\pi\zeta\omega_0/\omega_d} \;=\; \mathrm{e}^{-\pi\lambda}. \tag{S100}$$

For the calibrated binary collision,

$$\lambda_{\mathrm{bin}}(e) \;=\; -\frac{\ln e}{\pi}. \tag{S101}$$

The frequency definitions also give

$$\omega_0^2 \;=\; \omega_d^2+(\zeta\omega_0)^2. \tag{S102}$$

Dividing Equation (S102) by ω_d^2, with the last term equal to λ^2 by Equation (S97), gives

$$\frac{\omega_0^2}{\omega_d^2} \;=\; 1 + \frac{(\zeta\omega_0)^2}{\omega_d^2} \;=\; 1 + \lambda^2. \tag{S103}$$

Thus,

$$\frac{\omega_d}{\omega_0} \;=\; \frac{1}{\sqrt{1+\lambda^2}}. \tag{S104}$$

Multiplying Equation (S97) by ω_d/ω_0 gives the generic relation between λ and ζ. Applying it to the binary calibration yields

$$\zeta \;=\; \frac{\lambda}{\sqrt{1+\lambda^2}}, \qquad \zeta_{\mathrm{bin}}(e) \;=\; \frac{-\ln e}{\sqrt{\pi^2 + (\ln e)^2}}. \tag{S105}$$

Equivalently,

$$1 - \zeta^2 \;=\; 1 - \frac{\lambda^2}{1+\lambda^2} \;=\; \frac{1}{1+\lambda^2}. \tag{S106}$$

For $e = 0.5$,

$$\lambda_{\mathrm{bin}} \;=\; -\frac{\ln 0.5}{\pi} \;=\; 0.2206, \qquad \zeta_{\mathrm{bin}} \;=\; \frac{0.2206}{\sqrt{1+0.2206^2}} \;=\; 0.2154. \tag{S107}$$

S3.4 Exact map: damped Hertz to the linear oscillator

The nonlinear contact law can be mapped exactly onto the phase-space trajectory of the linear oscillator. The map preserves the orbit but not its physical time parametrization.

Introduce the transformed overlap

$$y \;=\; \delta^{5/4}. \tag{S108}$$

The required powers are

$$\delta \;=\; y^{4/5}, \qquad \delta^{1/4} \;=\; y^{1/5}, \qquad \delta^{3/2} \;=\; y^{6/5}, \qquad \delta^{5/2} \;=\; y^2. \tag{S109}$$

Treating $\dot\delta$ as a function of overlap and then changing variables from δ to y, the chain rule gives

$$\ddot\delta \;=\; \frac{d\dot\delta}{dt} \;=\; \frac{d\dot\delta}{d\delta}\frac{d\delta}{dt} \;=\; \dot\delta\,\frac{d\dot\delta}{d\delta} \;=\; \dot\delta\,\frac{d\dot\delta}{dy}\frac{dy}{d\delta}, \qquad \frac{dy}{d\delta} \;=\; \tfrac{5}{4}\,\delta^{1/4} \;=\; \tfrac{5}{4}\,y^{1/5}. \tag{S110}$$

The physical time derivative of the transformed overlap is

$$\dot y \;=\; \tfrac{5}{4}\,\delta^{1/4}\,\dot\delta. \tag{S111}$$

Substitution into Equation (S81) yields

$$m^*\,\dot\delta\,\frac{d\dot\delta}{dy}\cdot\tfrac{5}{4}\,y^{1/5} \;=\; -\,k_H\,y^{6/5} \;-\; \eta_0\,y^{1/5}\,\dot\delta. \tag{S112}$$

For $y > 0$, division by $y^{1/5}$ gives

$$\tfrac{5}{4}\, m^*\, \dot{\delta}\, \frac{d\dot{\delta}}{dy} \;=\; -\,k_H\, y \;-\; \eta_0\, \dot{\delta}. \tag{S113}$$

Define the auxiliary mass

$$\tilde{m} \;\equiv\; \tfrac{5}{4}\, m^*. \tag{S114}$$

For the auxiliary linear oscillator, writing acceleration as $\ddot{y} = \dot{y}\, d\dot{y}/dy$ gives its phase-space equation

$$\tilde{m}\, \dot{y}\, \frac{d\dot{y}}{dy} \;=\; -\,k_H\, y \;-\; \eta_0\, \dot{y}. \tag{S115}$$

Equations (S113) and (S115) are identical under the state-space identification $(y, \dot{\delta}) \leftrightarrow (y, \dot{y})$. They also share the initial state $(0, \dot{\delta}_0)$, so they trace the same orbit. This statement concerns the orbit only: the physical derivative of $y = \delta^{5/4}$ is given by Equation (S111) and is not generally equal to $\dot{\delta}$. The nonlinear contact and the auxiliary oscillator therefore traverse the same phase-space curve at different rates. Endpoint quantities, such as restitution, and extrema taken over the orbit, such as the peak contact force, are nevertheless identical.

S3.5 Peak total force of a binary damped contact: $\Psi_{\mathsf{bin}}(e)$

We now evaluate the maximum total contact force for the binary collision. The trapped three-body configuration will use the same result with a different effective damping ratio.

Because fracture is triggered by force, the relevant quantity is the total compressive force transmitted by the spring and dashpot. Using $y = \delta^{5/4}$,

$$F_{\mathsf{tot}} \;=\; k_H\, \delta^{3/2} + \eta_0\, \delta^{1/4}\dot{\delta} \;=\; \delta^{1/4}\big(k_H\, \delta^{5/4} + \eta_0 \dot{\delta}\big) \;=\; y^{1/5}\, \big(k_H\, y + \eta_0 \dot{\delta}\big). \tag{S116}$$

The factor $y^{1/5}$ means that the maximum of F_{tot} is not simply the maximum of the linear combination in parentheses.

Along the shared phase-space orbit, substitute the oscillator expressions for y and the paired velocity $\dot{\delta}$ into the bracketed term:

$$k_H y + \eta_0 \dot{\delta} \;=\; \dot{\delta}_0\, \mathrm{e}^{-\zeta\omega_0 t}\Big[\Big(\frac{k}{\omega_d} - \frac{\eta_0\, \zeta\omega_0}{\omega_d}\Big)\, \mathsf{sin}(\omega_d t) + \eta_0\, \mathsf{cos}(\omega_d t)\Big]. \tag{S117}$$

The identity

$$\omega_0^2 - 2(\zeta\omega_0)^2 \;=\; \omega_d^2 + (\zeta\omega_0)^2 - 2(\zeta\omega_0)^2 \;=\; \omega_d^2 - (\zeta\omega_0)^2, \tag{S118}$$

together with $k_H = \tilde{m}\omega_0^2$ and $\eta_0 = 2\tilde{m}\zeta\omega_0$, reduces Equation (S117) to

$$k_H y + \eta_0 \dot{\delta} \;=\; \frac{\tilde{m}\dot{\delta}_0}{\omega_d}\, \mathrm{e}^{-\zeta\omega_0 t}\Big[\big(\omega_d^2 - (\zeta\omega_0)^2\big)\, \mathsf{sin}(\omega_d t) + 2\zeta\omega_0\, \omega_d\, \mathsf{cos}(\omega_d t)\Big]. \tag{S119}$$

The sine and cosine coefficients in Equation (S119) have resultant amplitude ω_0^2, since

$$\left(\omega_d^2 - (\zeta\omega_0)^2\right)^2 + (2\zeta\omega_0\,\omega_d)^2 \;=\; \omega_d^4 - 2\omega_d^2(\zeta\omega_0)^2 + (\zeta\omega_0)^4 + 4(\zeta\omega_0)^2\omega_d^2 \;=\; \left(\omega_d^2 + (\zeta\omega_0)^2\right)^2 \;=\; \omega_0^4. \tag{S120}$$

Using the addition formula, for any angles β and β',

$$\sin(\beta+\beta') \;=\; \sin\beta\,\cos\beta' \;+\; \cos\beta\,\sin\beta', \tag{S121}$$

define the force phase advance τ_F by

$$\cos\tau_F \;=\; \frac{\omega_d^2 - (\zeta\omega_0)^2}{\omega_0^2}, \qquad \sin\tau_F \;=\; \frac{2\zeta\omega_0\,\omega_d}{\omega_0^2}. \tag{S122}$$

Then

$$\begin{aligned} \omega_0^2\,\sin(\omega_d t+\tau_F) \;&=\; \omega_0^2\left[\sin(\omega_d t)\cos\tau_F + \cos(\omega_d t)\sin\tau_F\right] \\ &=\; \left(\omega_d^2 - (\zeta\omega_0)^2\right)\sin(\omega_d t) + 2\zeta\omega_0\,\omega_d\cos(\omega_d t). \end{aligned} \tag{S123}$$

Substitution into Equation (S119) gives

$$k_H y + \eta_0\dot\delta \;=\; \frac{\tilde m\dot\delta_0\,\omega_0^2}{\omega_d}\,\mathrm{e}^{-\zeta\omega_0 t}\,\sin(\omega_d t+\tau_F). \tag{S124}$$

To express τ_F in terms of the damping index, note that

$$\zeta\omega_0 \;=\; \lambda\,\omega_d, \qquad \frac{\omega_d^2}{\omega_0^2} \;=\; \frac{1}{1+\lambda^2}. \tag{S125}$$

Therefore,

$$\cos\tau_F \;=\; \frac{(1-\lambda^2)\,\omega_d^2}{\omega_0^2} \;=\; \frac{1-\lambda^2}{1+\lambda^2}, \qquad \sin\tau_F \;=\; \frac{2\lambda\,\omega_d^2}{\omega_0^2} \;=\; \frac{2\lambda}{1+\lambda^2}. \tag{S126}$$

The double-angle identities in tangent form are, for any angle β,

$$\cos 2\beta \;=\; \frac{1-\tan^2\beta}{1+\tan^2\beta}, \qquad \sin 2\beta \;=\; \frac{2\tan\beta}{1+\tan^2\beta}. \tag{S127}$$

Setting $\beta = \arctan\lambda$ gives

$$\cos(2\arctan\lambda) \;=\; \frac{1-\lambda^2}{1+\lambda^2}, \qquad \sin(2\arctan\lambda) \;=\; \frac{2\lambda}{1+\lambda^2}. \tag{S128}$$

Equations (S126) and (S128) have the same sine and cosine. Choosing the physical branch $0 \le \tau_F < \pi$ therefore gives

$$\tau_F \;=\; 2\arctan\lambda. \tag{S129}$$

Introduce the dimensionless phase

$$\tau \;\equiv\; \omega_d t, \qquad \zeta\omega_0\,t \;=\; \lambda\,\tau. \tag{S130}$$

Equation (S96) then gives

$$y^{1/5} \;=\; \left(\frac{\dot\delta_0}{\omega_d}\right)^{1/5}\mathrm{e}^{-\lambda\tau/5}\,(\sin\tau)^{1/5}. \tag{S131}$$

Similarly, Equation (S124) becomes

$$k_H\, y + \eta_0 \dot{\delta} \;=\; k_H\, \frac{\dot{\delta}_0}{\omega_d}\, \mathrm{e}^{-\lambda\tau}\, \sin(\tau + \tau_F). \tag{S132}$$

Multiplying Equations (S131) and (S132) according to Equation (S116) yields

$$\begin{aligned} F_{\mathrm{tot}}(\tau) \;&=\; \Big(\frac{\dot{\delta}_0}{\omega_d}\Big)^{1/5} \mathrm{e}^{-\lambda\tau/5}\, (\sin\tau)^{1/5} \;\cdot\; k_H\, \frac{\dot{\delta}_0}{\omega_d}\, \mathrm{e}^{-\lambda\tau}\, \sin(\tau + \tau_F) \\ &=\; k_H \Big(\frac{\dot{\delta}_0}{\omega_d}\Big)^{6/5} \mathrm{e}^{-\frac{6}{5}\lambda\tau}\, (\sin\tau)^{1/5}\, \sin(\tau + \tau_F). \end{aligned} \tag{S133}$$

During compressive loading, $0 < \tau < \pi - \tau_F$, both sine factors in Equation (S133) are positive. The force vanishes at the two endpoints, so its maximum lies in the interior. Because the logarithm is monotone, the maximizing phase is obtained more conveniently from

$$\ln F_{\mathrm{tot}} \;=\; \ln\Big[k_H \Big(\tfrac{\dot{\delta}_0}{\omega_d}\Big)^{6/5}\Big] \;-\; \tfrac{6}{5}\,\lambda\tau \;+\; \tfrac{1}{5}\ln\sin\tau \;+\; \ln\sin(\tau + \tau_F). \tag{S134}$$

The required logarithmic derivative is

$$\frac{d}{d\tau}\, \ln\sin\tau \;=\; \frac{\cos\tau}{\sin\tau} \;\equiv\; \cot\tau. \tag{S135}$$

Differentiating Equation (S134) therefore gives

$$\frac{d\,\ln F_{\mathrm{tot}}}{d\tau} \;=\; -\tfrac{6}{5}\,\lambda \;+\; \tfrac{1}{5}\cot\tau \;+\; \cot(\tau + \tau_F). \tag{S136}$$

Let τ_{pk} denote the phase of the force maximum. Setting Equation (S136) to zero gives

$$\tfrac{1}{5}\cot\tau_{\mathrm{pk}} \;+\; \cot(\tau_{\mathrm{pk}} + \tau_F) \;=\; \tfrac{6}{5}\,\lambda. \tag{S137}$$

On $0 < \tau < \pi - \tau_F$, both cotangent terms decrease strictly. The left-hand side therefore decreases from $+\infty$ to $-\infty$, so Equation (S137) has exactly one root. This root is obtained numerically.

In the lossless limit, $\lambda = 0$, $\tau_F = 0$, and $\omega_d = \omega_0$. Equation (S133) is then proportional to $(\sin\tau)^{6/5}$ and reaches its maximum at $\tau = \pi/2$:

$$F_{\mathrm{max}}^{\mathrm{undamped}} \;=\; k_H \Big(\frac{\dot{\delta}_0}{\omega_0}\Big)^{6/5}. \tag{S138}$$

Using $\omega_0 = \sqrt{k/\tilde{m}}$ and $\tilde{m} = \frac{5}{4}\, m^*$,

$$k_H \Big(\frac{\dot{\delta}_0}{\omega_0}\Big)^{6/5} \;=\; k_H \left(\frac{\tilde{m}}{k}\right)^{3/5} \dot{\delta}_0^{6/5} \;=\; k_H^{2/5} \big(\tfrac{5}{4}\, m^*\big)^{3/5}\, \dot{\delta}_0^{6/5}, \tag{S139}$$

which reproduces Equation (S74). Dividing Equation (S133) at τ_{pk} by Equation (S138) gives

$$\Psi \;=\; \Big(\frac{\omega_0}{\omega_d}\Big)^{6/5} \mathrm{e}^{-\frac{6}{5}\lambda\tau_{\mathrm{pk}}}\, (\sin\tau_{\mathrm{pk}})^{1/5}\, \sin(\tau_{\mathrm{pk}} + \tau_F). \tag{S140}$$

Using $1-\zeta^2=(1+\lambda^2)^{-1}$ and $\tau_F=2\arctan\lambda$, the binary-collision force factor can be written as

$$\Psi_{\mathrm{bin}}(e) \;=\; \bigl(1+\lambda_{\mathrm{bin}}^2\bigr)^{3/5}\mathrm{e}^{-\frac{6}{5}\lambda_{\mathrm{bin}}\tau_{\mathrm{pk}}}\,(\sin\tau_{\mathrm{pk}})^{1/5}\,\sin\bigl(\tau_{\mathrm{pk}}+2\arctan\lambda_{\mathrm{bin}}\bigr), \tag{S141}$$

where $\lambda_{\mathrm{bin}}(e)=-\ln e/\pi$, and τ_{pk} is the unique solution of Equation (S137) evaluated at $\lambda=\lambda_{\mathrm{bin}}$. For $e=0.5$, $\tau_F=0.434$, $\tau_{\mathrm{pk}}=1.001$, and $\Psi_{\mathrm{bin}}=0.756$.

S3.6 The trapped three-body configuration: $\Psi_{\mathrm{trap}}(e,R)$

We now apply the binary-contact result to the trapped ball–particle–ball compression mode. The two identical contacts act in series, while the inertia is supplied by the incoming grinding ball.

Let x be the displacement of the incoming ball toward the fixed ball and u the displacement of the target-particle center. The two contact overlaps are

$$\delta_1 \;=\; u, \qquad \delta_2 \;=\; x-u. \tag{S142}$$

In the head-on quasi-static approximation, the trapped particle is a two-force body, so the two identical contacts transmit the same force. Because they obey the same constitutive law and begin at zero overlap, their overlap histories are identical. Hence each contact accommodates half of the incoming ball's displacement:

$$\delta_1=\delta_2\equiv\delta=\frac{x}{2}, \qquad \dot\delta=\frac{\dot x}{2}. \tag{S143}$$

Newton's second law for the incoming ball is therefore

$$m_g\,\ddot x \;=\; -\,k_H\Bigl(\frac{x}{2}\Bigr)^{3/2}-\eta_0\Bigl(\frac{x}{2}\Bigr)^{1/4}\frac{\dot x}{2} \;=\; -\,\frac{k}{2^{3/2}}\,x^{3/2}-\frac{\eta_0}{2^{5/4}}\,x^{1/4}\dot x. \tag{S144}$$

This equation has the same form as Equation (S81) under the replacements

$$\bigl(m^*,\;k_H,\;\eta_0\bigr) \;\longrightarrow\; \Bigl(m_g,\;\frac{k}{2^{3/2}},\;\frac{\eta_0}{2^{5/4}}\Bigr). \tag{S145}$$

The binary-contact result therefore remains applicable after replacing the binary damping ratio by that of the trapped mode. For any underdamped mode,

$$\lambda \;=\; \frac{\zeta}{\sqrt{1-\zeta^2}}. \tag{S146}$$

For a Hertz oscillator with inertia m_{osc}, stiffness k_{spr}, and dashpot coefficient η, the auxiliary mass of Equation (S114) is $\frac{5}{4}m_{\mathrm{osc}}$ and the damping ratio is

$$\zeta \;=\; \frac{\eta}{2\sqrt{\frac{5}{4}\,m_{\mathrm{osc}}\,k_{\mathrm{spr}}}}. \tag{S147}$$

The target-particle to grinding-ball mass ratio is

$$\frac{m_t}{m_g} \;=\; \frac{\rho_t}{\rho_g}\Bigl(\frac{r_t}{r_g}\Bigr)^3 \;=\; \frac{\rho_t}{\rho_g R^3} \;\approx\; \frac{1}{185} \qquad \text{for } R=4, \tag{S148}$$

where the final value uses the densities $\rho_t = 2700$ and $\rho_g = 7800\ \mathrm{kg\,m^{-3}}$ of Table 1. The reduced mass used in the binary restitution calibration is

$$m^* \;=\; \frac{m_t m_g}{m_t + m_g} \;\approx\; \frac{185}{186}\, m_t \qquad \text{for } R = 4. \tag{S149}$$

Because LAMMPS calibrates η_0 using this binary reduced mass,

$$\zeta_{\mathrm{bin}}(e) \;=\; \frac{\eta_0}{2\sqrt{\frac{5}{4}\, m^* k_H}} \;=\; \frac{-\ln e}{\sqrt{\pi^2 + (\ln e)^2}}. \tag{S150}$$

For the trapped mode, Equations (S145) and (S147) give

$$\begin{aligned} \zeta_{\mathrm{trap}} \;&=\; \frac{\eta_0 / 2^{5/4}}{2\sqrt{\frac{5}{4}\, m_g (k_H / 2^{3/2})}} \\ &=\; \frac{\eta_0}{2\sqrt{\frac{5}{4}\, m^* k_H}} \sqrt{\frac{m^*}{2m_g}} \;=\; \zeta_{\mathrm{bin}}(e) \sqrt{\frac{m^*}{2m_g}}. \end{aligned} \tag{S151}$$

Using the exact reduced mass from Equation (S71),

$$\zeta_{\mathrm{trap}}(e, R) \;=\; \zeta_{\mathrm{bin}}(e) \sqrt{\frac{m_t}{2\big(m_t + m_g\big)}}. \tag{S152}$$

Equivalently, in terms of density and size ratio,

$$\zeta_{\mathrm{trap}}(e, R) \;=\; \zeta_{\mathrm{bin}}(e) \sqrt{\frac{\rho_t}{2\big(\rho_t + \rho_g R^3\big)}} \;\simeq\; \zeta_{\mathrm{bin}}(e) \sqrt{\frac{\rho_t}{2\rho_g}}\, R^{-3/2}, \tag{S153}$$

where the approximation uses $m_g \gg m_t$. The densities are fixed material parameters and are therefore suppressed from the argument list of $\Psi_{\mathrm{trap}}(e, R)$. At $e = 0.5$ and $R = 4$,

$$\zeta_{\mathrm{trap}} \;=\; 0.2154 \sqrt{\frac{1}{372}} \;=\; 0.0112. \tag{S154}$$

Define the effective damping index of the trapped mode by

$$\lambda_{\mathrm{trap}} \;\equiv\; \frac{\zeta_{\mathrm{trap}}}{\sqrt{1 - \zeta_{\mathrm{trap}}^2}}. \tag{S155}$$

The phase τ_{pk} at which the transmitted force is maximal is the unique numerical solution of

$$\frac{1}{5} \cot \tau_{\mathrm{pk}} + \cot(\tau_{\mathrm{pk}} + 2 \arctan \lambda_{\mathrm{trap}}) \;=\; \frac{6}{5} \lambda_{\mathrm{trap}}, \qquad 0 < \tau_{\mathrm{pk}} < \pi - 2 \arctan \lambda_{\mathrm{trap}}. \tag{S156}$$

Because λ_{trap} is far smaller than λ_{bin}, this root differs from the binary one: at $e = 0.5$ and $R = 4$ it is $\tau_{\mathrm{pk}} = 1.54$, close to the lossless $\pi/2$, rather than the binary value 1.001. Substituting these quantities into the binary-contact result gives the damping factor for the trapped three-body configuration:

$$\Psi_{\mathrm{trap}}(e, R) \;=\; \big(1 + \lambda_{\mathrm{trap}}^2\big)^{3/5} \mathrm{e}^{-\frac{6}{5} \lambda_{\mathrm{trap}} \tau_{\mathrm{pk}}} \big(\sin \tau_{\mathrm{pk}}\big)^{1/5} \sin(\tau_{\mathrm{pk}} + 2 \arctan \lambda_{\mathrm{trap}})\,. \tag{S157}$$

For $e = 0.5$ and $R = 4$, Equation (S157) gives $\Psi_{\text{trap}} = 0.979$. Therefore,

$$v_{c,\text{damp}} \;=\; v_{c,0}\,\Psi_{\text{trap}}^{-5/6} \;=\; 1.017\,v_{c,0}, \tag{S158}$$

so damping raises the predicted head-on fracture threshold by approximately 1.7%.

The threshold is correspondingly insensitive to the value adopted for e. Evaluating Equation (S157) across the plausible range gives a correction of 3.7% at $e = 0.2$, falling monotonically to 0.3% at $e = 0.9$, so the predicted threshold changes by less than 2% relative to its value at $e = 0.5$ anywhere in that range. At fixed $e = 0.5$ the correction depends more strongly on size ratio, from 4.9% at $R = 2$ to 0.16% at $R = 20$, because the trapped mode is more heavily damped when the target particle is a larger fraction of the grinding-ball mass.

A direct DEM test of this result is shown in Fig. 5 of the main text.

S4 Numerical convergence of the recording interval

The failure functions are evaluated from simulation output recorded every 100 timesteps, and the recorded maximum could in principle miss the true force peak between two outputs. To test this, three head-on collisions at $v = 0.95\, v_c$, v_c, and $1.05\, v_c$ ($R = 4$, $\mu = 0.47$) were rerun with output recorded at every timestep, and the peak failure functions were then re-evaluated on subsampled versions of the same trajectories at recording intervals $N = 1$ to 400. Figure S1 shows the recovered peaks, normalized by the every-timestep value: at the production interval $N = 100$ both criteria are converged to within 0.1%, and visible deviations appear only beyond $N \approx 200$.

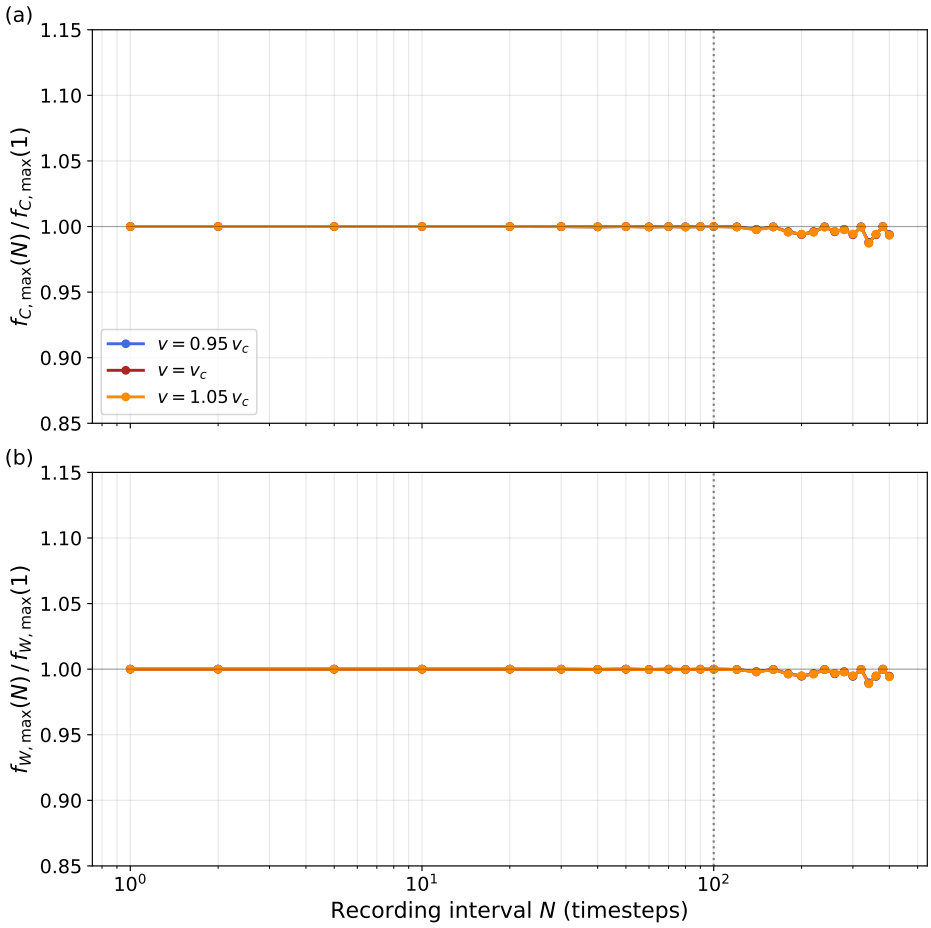


Figure S1: Sensitivity of the recorded peak failure functions to the recording interval N, for (a) the Christensen criterion and (b) the Weibull criterion, at head-on impact velocities $0.95\, v_c$ (blue circles), v_c (dark red circles), and $1.05\, v_c$ (orange circles), with $R = 4$ and $\mu = 0.47$. Each curve shows the peak failure function recovered at recording interval N, normalized by its value at $N = 1$; an interval of N timesteps corresponds to $0.1N$ μs. The dotted vertical line marks the production interval $N = 100$.